

IGRINS RV: A Precision Radial Velocity Pipeline for IGRINS Using Modified Forward Modeling in the Near-infrared*

Asa G. Stahl¹, Shih-Yun Tang^{2,3}, Christopher M. Johns-Krull¹, L. Prato^{2,3}, Joe Llama², Gregory N. Mace⁴, Jae Joon Lee⁵, Heeyoung Oh⁵, Jessica Luna⁴, and Daniel T. Jaffe⁴, Department of Physics and Astronomy, Rice University, 6100 Main Street, Houston, TX 77005, USA; Asa.Stahl@rice.edu

1 Department of Physics and Astronomy, Rice University, 6100 Main Street, Houston, TX 77005, USA; Asa.Stahl@rice.edu

2 Lowell Observatory, 1400 West Mars Hill Road, Flagstaff, AZ 86001, USA; sytang@lowell.edu

3 Department of Astronomy and Planetary Sciences, Northern Arizona University, Flagstaff, AZ 86011, USA

4 Department of Astronomy, University of Texas at Austin, 2515 Speedway, Austin, TX, USA

5 Korea Astronomy and Space Science Institute, 776 Daedeokdae-ro, Yuseong-gu, Daejeon 34055, Republic of Korea

Received 2021 February 1; revised 2021 March 30; accepted 2021 April 5; published 2021 May 26

Abstract

Application of the radial velocity (RV) technique in the near-infrared is valuable because of the diminished impact of stellar activity at longer wavelengths, making it particularly advantageous for the study of late-type stars but also for solar-type objects. In this paper, we present the IGRINS RV open-source python pipeline for computing infrared RV measurements from reduced spectra taken with IGRINS, an $R \equiv \lambda/\Delta\lambda \sim 45,000$ spectrograph with simultaneous coverage of the H band (1.49–1.80 μ m) and K band (1.96–2.46 μ m). Using a modified forward-modeling technique, we construct high-resolution telluric templates from A0 standard observations on a nightly basis to provide a source of common-path wavelength calibration while mitigating the need to mask or correct for telluric absorption. Telluric standard observations are also used to model the variations in instrumental resolution across the detector, including a yearlong period when the K band was defocused. Without any additional instrument hardware, such as a gas cell or laser frequency comb, we are able to achieve precisions of 26.8 m s⁻¹ in the K band and 31.1 m s⁻¹ in the K band for narrow-line hosts. These precisions are empirically determined by a monitoring campaign of two RV standard stars, as well as the successful retrieval of planet-induced RV signals for both HD 189733 and τ Boo A; furthermore, our results affirm the presence of the Rossiter–McLaughlin effect for HD 189733. The IGRINS RV pipeline extends another important science capability to IGRINS, with publicly available software designed for widespread use.

Unified Astronomy Thesaurus concepts: Exoplanet detection methods (489); Exoplanet formation (492); Radial velocity (1332); Near infrared astronomy (1093); Open source software (1866); Astronomy software (1855); Starspots (1572); Young stellar objects (1834)

Supporting material: machine-readable table

Software reviewed by the Journal of Open Source Software JOSS

1. Introduction

The radial velocity (RV) method is a powerful tool for detecting planets around other stars. Ever since the analysis of RV variations facilitated the first detection of an exoplanet around a Sun-like star (51 Pegasi b; Mayor & Queloz 1995), the technique has remained one of the major workhorses for exoplanet discovery and characterization (Akeson et al. 2013). RV analysis is the only nonserendipitous exoplanet detection method that provides an independent determination of a planet's mass, an essential parameter for planet characterization. RV variations can also directly measure a planet's orbital eccentricity. This is often studied in connection with dynamical evolution and planet formation pathways (Morishima et al. 2008; Wang et al. 2017).

In concert with transit observations, RV measurements make it possible to estimate the bulk densities of planets (Marcy et al. 2014) and to measure spin-orbit angles through the Rossiter-McLaughlin effect (Collier Cameron et al. 2010; Triaud 2018). At the same time, planet-induced RV signals are less dependent on orbital period and inclination than transit signals (Martin et al. 2019). RV surveys are thus important for probing the range of potential planetary system architectures.

RVs measured in the infrared, as opposed to the optical, extend the capabilities of the method. For one, they provide a better means for planet searches around M dwarfs, which emit the most light in the near-infrared (NIR; Plavchan et al. 2015). These stars are increasingly attractive targets for exoplanet detection efforts on account of their abundance in the Milky Way (Henry et al. 2006); the increased detectability of small planets around small stars (Günther et al. 2020); their closer, more easily probed habitable zones (France et al. 2016); and their amenability to planetary atmospheric characterization (Ballard 2019).

Infrared RVs also exhibit diminished wavelength-dependent stellar jitter, such as those induced by starspots (Robertson et al. 2020; Tran et al. 2021). As the radiation of both a star and a starspot generally follows a Planck distribution, at wavelengths greater than that of their peak emission, the contrast between a spot and its host star will diminish. Studies confirming this effect (Huélamo et al. 2008; Mahmud et al. 2011; Bailey et al. 2012) have found that RV spot modulation lowers by a factor of \sim 3 or more when moving from the optical to the H and K bands. Because planet-induced RV variations are wavelength independent, comparing measured RVs in the optical and NIR provides a robust means of diagnosing spot-induced false positives.

The capacity of NIR RVs to identify and/or diminish the relative magnitude of RV variations caused by stellar processes

^{*} https://github.com/shihyuntang/igrins_rv

means that they are useful for detecting planets around spotted FGKM stars and, notably, young stars. Pre-main-sequence stars within the mass regime of the Sun, known as T Tauri stars, are highly active, and their spotted surfaces and variable accretion can easily drown out otherwise observable planetary signals (Crockett et al. 2012). The strong magnetic activity of T Tauri stars (Johns-Krull 2007) can drive clumpy accretion and generate surface spots that obscure or mimic planetary signals, for example, through apparent RV fluctuations with semiamplitudes on the order of km s⁻¹ at optical wavelengths (Huerta et al. 2008; Dumusque et al. 2014). Even optical signals as large as that of a 20 $M_{\rm Jup}$ companion orbiting 0.2 au from a 0.6 M_{\odot} host star (a semiamplitude of 1 km s⁻¹) can be overwhelmed by typical T Tauri activity (e.g., Prato et al. 2008).

Several planet candidates around young stars have been detected over the past decade (e.g., van Eyken et al. 2012; Kraus et al. 2014; Sallum et al. 2015; Donati et al. 2016; Oelkers et al. 2016). The first planet around a T Tauri star young enough to still host its disk was confirmed last year via direct detection of CO in the planet (Flagg et al. 2019). Additional discoveries of planets around young stars are expected to help clarify the nature of planet formation (Livingston et al. 2018; Vanderburg et al. 2018), migration (Dawson & Johnson 2018), and photoevaporative atmospheric loss (David et al. 2019) through their direct probing of systems while such processes are ongoing. Over the past several years, several spectrographs dedicated to planet detection in the infrared have come online, including HPF (Mahadevan et al. 2012), IRD (Kotani et al. 2014), and CARMENES (Bauer et al. 2020). New infrared spectrographs like iSHELL (Rayner et al. 2016), while not designed for precise RV measurements, are also demonstrating sufficient RV precision to detect shortperiod and massive planets (e.g., Plavchan et al. 2020), continuing the progress made with legacy instruments such as CSHELL (e.g., Crockett et al. 2012) and CRIRES (e.g., Bean et al. 2010).

In this paper, we present IGRINS RV: a precision RV analysis pipeline for the Immersion GRating INfrared Spectrometer (IGRINS; Yuk et al. 2010; Park et al. 2014; Mace et al. 2016b, 2018). IGRINS is a compact and mobile IR spectrometer that has enabled a variety of science on three different telescopes so far. Its large spectral grasp and high resolution facilitate a vast array of applications, from exoplanet detection (Mann et al. 2016) and atmospheric characterization (Llama et al. 2019) to studies of stars (Sterling et al. 2016), the interstellar medium (Kaplan et al. 2017), and galaxies (Guerço et al. 2019).

Only a few cases of RV analysis have been performed with IGRINS so far. Using a cross-correlation technique, Carleo et al. (2018) report typical external RV uncertainties of 59 m s⁻¹, but they do not monitor an RV standard star to characterize the internal precision of their method; thus, their total, long-term RV precision is unknown. Another published analysis employing cross-correlation achieves robust median uncertainties of 150 m s⁻¹ (Mace et al. 2016a). Lastly, Johns-Krull et al. (2016) applied a forward-modeling technique using a static telluric template to achieve a precision of 75 m s⁻¹. IGRINS RV represents a more sophisticated continuation of this forward-modeling methodology, whose previous versions have also been effectively applied to CSHELL and PHOENIX spectra in the past (Crockett et al. 2012). The code will allow anyone to process IGRINS data to final RVs with nearly 3

times better precision than these previous studies, in an entirely self-contained package easily run from the command line.

IGRINS is a powerful instrument with a wide variety of science capabilities. At the same time, it is not temperature controlled at the level required for $\sim\!m\,s^{-1}\,RVs$, is not fiber fed, and does not have a built-in gas cell, laser frequency comb, or Fabry–Perot etalons—in short, it was not designed for precise RV experiments. IGRINS RV calculates precise NIR RVs through a modified forward-modeling technique in which a data-driven synthetic telluric template leverages atmospheric absorption lines as a wavelength calibrator. The methodology by which it does this is novel and could potentially be applied to other spectrographs.

The structure of this paper is as follows: in Section 2, we describe the data used in testing and validating the pipeline; in Section 3, we outline how the pipeline works; in Section 4, we present the results of applying our code to RV standard stars and known planet hosts; in Section 5, we summarize our findings and describe their future prospects.

Throughout this paper, we refer to each spectrum taken in a nodding sequence (e.g., A) as an "observation" and the collection of all observations in a sequence (e.g., AB or ABBA) as an "exposure."

2. Observations and Data Reduction

IGRINS is a high-resolution ($R \equiv \lambda/\Delta\lambda \sim 45,000$) cross-dispersed echelle spectrograph with a broad spectral grasp covering the full H band (1.49–1.80 μ m) and K band (1.96–2.46 μ m) simultaneously (Yuk et al. 2010; Park et al. 2014; Mace et al. 2016b, 2018). The former is split into 28 orders, and the latter is split into 26 orders, where each order corresponds to \sim 240 Å and consists of 2048 pixels. The H and K bands are imaged on two separate detectors.

IGRINS saw first light on McDonald Observatory's 2.7 m Harlan J. Smith Telescope in 2014. It was then moved to the Lowell Discovery Telescope (LDT; formerly the Discovery Channel Telescope, DCT) in 2016 August. Currently, IGRINS is available as a visiting instrument at the Gemini South Telescope. In this paper, we only use data taken while IGRINS was mounted at McDonald Observatory (McD) and at Lowell Observatory.

Spectra taken at the DCT included information on environmental conditions in their fits headers, such as the ambient humidity and temperature during an observation, but spectra taken at McD lacked these data. This led to a slightly different treatment of the observations when constructing telluric templates.

Observing logs for science targets can be found in Tables B1 and B2. The telluric standards used are listed in Table B3.

2.1. IGRINS K-band Defocus

Between 2018 January and 2019 August, IGRINS exhibited a change in spectral resolving power in the K band as the result of loose fasteners on the back of the detector mount. Figure 1 shows how the effect of this defocus varied over the detector. The largest change to the echellogram, in which the spectral resolution was reduced to $R \sim 20,000$, occurs in the shortwavelength end of the long-wavelength K-band orders (wavelengths on the IGRINS detector increase with increasing detector column and toward lower spectral orders). This is where the CO band heads are located ($\lambda > 2.3 \ \mu m$). While only

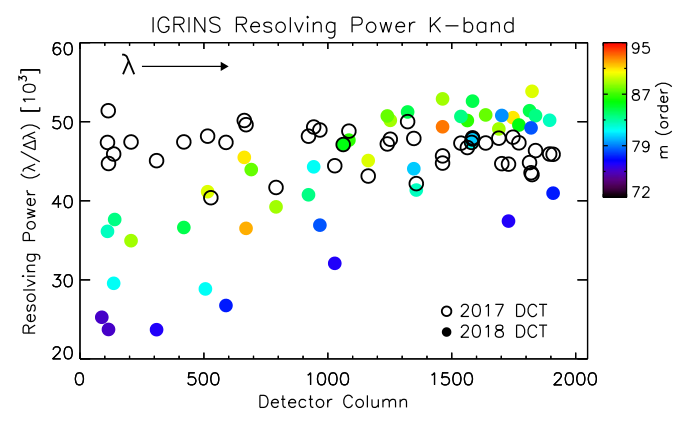


Figure 1. IGRINS spectral degradation in K band measured from the FWHM of sky OH emission lines, showing the changes in spectral resolution between 2017 and 2018 as a function of detector column and the diffraction order (m) on the detector.

two epochs are shown here, we have verified that these trends persist across many nights.

The defocus affected all data taken during the 2018 visit to Gemini and the subsequent visit to the DCT. In 2019 August, all fasteners on the K-band detector mount were repinned and tightened in the lab at the University of Texas at Austin. Cold testing showed that the echellogram focus was corrected back to the original design specifications (Yuk et al. 2010; Park et al. 2014). The H-band detector was also moved away from its camera by 200 μ m to achieve better focus. Laboratory testing at Gemini South in 2020 February, prior to recommissioning and after shipment from UT Austin, confirmed that the IGRINS H-and K-band echellograms remained at optimal focus.

The strategies IGRINS RV uses to mitigate the impact of the defocus are described in Sections 3.6 and 3.7.

2.2. Data Reduction and Flux Suppression Effect

We employed the IGRINS pipeline package version 2.2.0 (plp v2.2.0; Lee et al. 2017) to reduce our data from a raw format to one-dimensional spectra. While this reduction pipeline generates a wavelength solution, it is not the final wavelength solution used by IGRINS RV, as will be discussed in Section 3.

To facilitate robust uncertainty estimates in our RV measurements, we performed the extraction of the individual A and B frames of our observations separately. Because the A and B observing settings produce different slit illuminations, we were able to accomplish this by instructing the reduction pipeline only to use the upper or lower half of the echellogram orders through its -frac-slit command flag.

In the process of optimizing the RVs estimated from these individual A and B frames, we noticed a subtle artifact in the data: reduced A frames often exhibited a discrete reduction in flux near the peak of the blaze (Figures 3(a) and (b)). While the exact cause of this artifact is not known at this time, the flux suppression appears to be the result of a hardware effect that is exacerbated by the way the current version of the reduction pipeline (plp v2.2.0) performs optimal extraction. While the cause will be diagnosed and addressed if possible, an upcoming release of the plp will fully correct for the effect. In the meantime, it is relatively straightforward to address the flux

reduction in our analysis (Section 3.4, Figure 3(c)). Once the plp is updated, a new version of IGRINS RV will be correspondingly released. This effect is not present in spectra reduced by plp in telluric-corrected mode.

2.3. RV Standards: GJ 281 and HD 26257

GJ 281 and HD 26257 are both recognized RV standard stars. Past monitoring has found GJ 281 (M0.0Ve, $v \sin i = 2.96 \text{ km s}^{-1}$; Lépine et al. 2013) to be nonvariable in RV to <12 m s⁻¹ (Endl et al. 2003) and HD 26257 (G2V, $v \sin i = 9.24 \text{ km s}^{-1}$; Houk & Swift 1999) to be nonvariable to <7 m s⁻¹ (Butler et al. 2017). Additional information on these stars can be found in Table 1.

Observations of GJ 281 took place mainly at DCT between 2016 December and 2019 March. Of 60 nights of observation, 22 took place during the IGRINS *K*-band defocus. We also drew on six nights of observations taken at McD between 2014 and 2015 November.

HD 26257 was observed a total of 34 times at DCT between 2016 November and 2018 January.

Both RV standards are relatively bright, so most exposures typically consisted of an AB nodding sequence, as opposed to, e.g., an ABBA sequence.

To assure the quality of the extracted RVs, we refrained from analyzing observations without an accompanying telluric standard taken within an air-mass difference of 0.3, nor did we analyze RV standard spectra with signal-to-noise ratio (S/N) lower than 50. These cuts left us with 60 total observations for GJ 281, 5 of which were taken at McD, and 33 observations for HD 26257. See Table B1 for details.

2.4. Known Planet Hosts

In addition to our RV standards, we tested the performance of IGRINS RV by applying it to two known planet-hosting stars, HD 189733 and τ Boo A.

2.4.1. HD 189733b

HD 189733b is a transiting $1.15 \pm 0.04 M_J$ planet in a \sim 2.219-day orbit around its host star. It was first detected by Bouchy et al. (2005) using the ELODIE fiber-fed optical spectrograph. This planetary system is in a nearly edge-on orientation with an inclination of $85^{\circ}.3 \pm 0^{\circ}.1$ and induces an RV semiamplitude in its host star of $205 \pm 6 \,\mathrm{m\,s^{-1}}$. Bakos et al. (2006) reported a distant M-dwarf companion with a projected separation of 11"2 and a period of ~3200 yr, but no follow-up studies have attempted to refine the stellar companion's orbital solution. Other than being a famous target for planetary atmospheric studies (Alonso-Floriano et al. 2019; Steinrueck et al. 2019), HD 189733b is also one of the few planetary systems exhibiting the Rossiter-McLaughlin effect. The system's transit-induced RV anomaly was first recognized by Bouchy et al. (2005) and has since been revisited with NIR observations using SPIRou (Moutou et al. 2020), who found the peak-to-peak amplitude of the anomaly to be $\sim 110 \text{ m s}^{-1}$. Other basic information on this target can be found in Table 1.

Observations of HD 189733 took place at McD between 2015 May and 2016 July and at DCT between 2016 October and 2017 September. All eight nights of observations taken were used. Given the short period of HD 189733b, each night of observation covered a large portion of its phase space. We therefore treated each exposure (i.e., each ABBA sequence) as

https://github.com/igrins/plp

Table 1 Test Target Basic Information

Target	R.A.	Decl.	SpTy	$T_{ m eff}$	log g	H(b)	K(b)	Distance(c)	Notes	RVª	$v \sin i^{a}$
	(hh:mm:ss)	(±dd:mm:ss)		(K)		(m	nag) (pc)			$(km s^{-1})$	
(1)	(2)	(3)	(4)	(5)	(6)	(7)	(8)	(9)	(10)	(11)	(12)
GJ 281	07:39:23.04	+02:11:01.2	M0.0Ve(d)	4014(^h)	4.66(^h)	6.09	5.87	15.05	RV Standard	20.08	2.96
HD 26257	04:09:09.07	+00:10:44.3	G2V(°)	6129(ⁱ)	4.31(ⁱ)	6.44	6.42	56.05	RV Standard	33.92	9.24
HD 189733	20:00:43.71	+22:42:39.1	$K2V(^{f})$	5023(ⁱ)	$4.51(^{i})$	5.59	5.54	19.76	Planet Host	•••	•••
au Boo A	13:47:15.74	+17:27: 24.9	F7IV-V(g)	6387(^j)	$4.27(^{i})$	3.55	3.36	15.65	Planet Host	•••	•••

Notes.

- ^a Determined by IGRINS RV (this study).
- ^b Skrutskie et al. (2006).
- ^c Bailer-Jones et al. (2018).
- d Lépine et al. (2013)
- e Houk & Swift (1999).
- Gray et al. (2003).
- ^g Gray et al. (2001).
- h Schweitzer et al. (2019).
- i Brewer et al. (2016).
- ^j Fischer & Valenti (2005).

a statistically independent RV measurement. Of 82 such measurements, we were able to extract 81 high-quality RVs.

$2.4.2. \tau Boo A b$

 τ Boo A b was one of the first exoplanets ever discovered (Butler et al. 1997). The gas giant has a roughly circular 3.31day orbit, inducing an RV semiamplitude of 461.1 \pm 7.6 m s⁻¹ (Butler et al. 2006). Two separate teams have estimated the inclination of the orbit to be $44^{\circ}.5 \pm 1^{\circ}.5$ (Brogi et al. 2012) and $47^{\circ} \pm 7^{\circ}$ (Rodler et al. 2012), corresponding to planetary masses of 5.95 \pm 0.28 M_I and 5.6 \pm 0.7 M_I , respectively.

A visual companion M star to τ Boo A is at a separation of 1.662 ± 0.002 (Justesen & Albrecht 2019). Several studies have tried to estimate the orbital solution for the $\tau \, \mathrm{Boo} \, \mathrm{AB}$ binary system (Hale 1994; Popović & Pavlović 1996), but these efforts have been complicated by poor orbital phase coverage as a result of the long period of the system. With over 150 yr of astrometric data and 25 yr of RV data, Justesen & Albrecht (2019) were unable to place precise constraints on the binary's orbital period or semimajor axis, estimating 2420^{+2587}_{-947} yr and 221^{+138}_{-62} au, respectively. However, the authors do confirm the eccentricity of the orbit at $0.87^{+0.04}_{-0.03}$, and their RV data provide a means through which one can account for the M dwarf's impact on the measured RVs of τ Boo A (Section 4.2). Besides affecting the actual velocity of $\tau Boo A$, we expect light from the M-dwarf companion to slightly contaminate IGRINS spectra of the target, given the instrument's slit width of 1" at McD and that the H-band magnitude difference between the two stars is \sim 4 mag based on their blackbody temperatures. Table 1 provides additional information on the planet host.

The observation of τ Boo A took place at McD over two epochs, the first lasting from 2015 January to July, and the second between 2016 February and March. As with HD 189733, the short period of the planetary companion and the intense monitoring cadence led us to divide each night into multiple independently analyzed ABBA exposures, such that the 16 nights of data yielded 217 RV measurements, of which 215 were of high enough quality to deliver reliable values.

3. The IGRINS RV Pipeline

3.1. Workflow

The IGRINS RV pipeline is divided into three main steps: Telluric Modeling, Initial Convergence, and Analysis. Each is provided in the package as a separate module, and each is run from the command line with keywords specifying all relevant information. A brief outline of each step follows.

Step 1—Telluric Modeling: Defines the wavelength regions to be analyzed; generates a synthetic, high-resolution telluric template for use in later model fits on a night-by-night and frame-by-frame (i.e., A vs. B) basis.

Step 2—Initial Convergence: Required if the average RV of the target star, or its $v \sin i$, is unknown to >5 km s⁻¹ precision. This step performs an abbreviated analysis of the target star observations in order to converge to coarsely accurate RVs, which will be used as starting points for the more precise analysis in the next step. It simultaneously does the same for the target star's $v \sin i$, if unknown. For the sake of expediency, only a single wavelength region (see Section 3.5) is used, and only a single B frame observation for every given exposure

Step 3—Analysis: Performs a full analysis of each target star observation to produce accurate and precise RVs. All the wavelength regions defined in Step 1 are used, and the code performs spectral fits of each observation that is part of a given exposure separately.

Unless the target $v \sin i$ is already known to high accuracy, an initial run of Step 3 in which $v \sin i$ is allowed to vary is required. This provides an estimate of $v \sin i$ that can then be plugged into the code as a fixed value in the second run of Step 3. If $v \sin i$ is already well known, it is not necessary to run Step 3 more than once, as the code fully converges to the final RVs (within uncertainty) through just one run.

3.2. Stellar Template Generation

The stellar templates used in the analyses presented in this paper were primarily produced with the SYNTHMAG C++ code (Kochukhov 2007) in concert with PHOENIX NextGen model atmospheres (Hauschildt et al. 1999) and the VALD

stellar line database (Ryabchikova et al. 2015). VALD line lists were generated with a detection threshold of 0.01, a microturbulence of 1 km s⁻¹, and solar chemical composition. The effective temperature and $\log g$ were set to within 200 K and 0.5 dex step sizes, respectively, of those of the target star in question.

For GJ 281, we used a synthetic stellar template with a $T_{\rm eff}$ of 4000 K and log g of 4.5; for HD 26257, we used a template with a $T_{\rm eff}$ of 6200 K and log g of 4.5. The HD 189733 analysis employed a template with a $T_{\rm eff}$ of 5000 K and log g of 4.5. For τ Boo A, we used a template with a $T_{\rm eff}$ of 6400 K and log g of 4.5.

It is not uncommon for RV experiments to construct a stellar template from observations (e.g., Cale et al. 2018). However, extraction of a stellar template from data requires computationally expensive iteration and disfavors the use of separate exposures for the sake of a combined, higher-S/N spectrum. Our ability to analyze separate exposures in a nodding sequence provides better characterization of our precision.

All templates used in this study are provided with the IGRINS RV package. This includes the four templates mentioned above, as well as several others used for testing the code. The models unevenly span a temperature range of 3000-6400 K and $\log g$ of 3.5-5.0. Users running the code on any target stars beyond the range of effective temperature or surface gravity of the handful of templates provided are strongly encouraged to supply their own stellar templates, as discussed in Section 4.3.

3.3. Telluric Template Generation

In the PHOENIX (Hinkle et al. 1998) and CSHELL (Greene et al. 1993) RV codes deployed in Johns-Krull et al. (2016), the telluric contribution to spectral absorption is modeled using the high-resolution ($R \sim 600,000$) atlas of the infrared solar spectrum taken with the Fourier Transform Spectrometer at the McMath/Pierce Solar Telescope on Kitt Peak (Livingston & Wallace 1991). Livingston & Wallace (1991) monitored the solar infrared spectrum over time and used the stellar absorption's variability to carefully distinguish it from telluric absorption. This isolated telluric spectrum is hereafter referred to as the "Livingston atlas."

The Livingston atlas was adequate when applied over the small wavelength ranges covered by CSHELL and PHOENIX (\sim 60 and \sim 115 Å, respectively), but when applied across several orders of IGRINS spectra, it results in large discrepancies between the model and the data, jeopardizing the accuracy of the model fits.

Pairing target observations with those of bright, featureless stars (typically type A0) can ameliorate this issue. One method is to use the A0 spectra themselves as telluric templates. Observed soon before or after the target star and at similar air masses and sky location, such A0 templates will have very similar telluric contributions to the target star spectra and will also exhibit comparable instrumental broadening. However, this strategy suffers from two major drawbacks: the A0 spectra are sampled at the same resolution as the target star spectra, such that the user's choice to interpolate the observed spectrum as a template will cause overinterpolation, and as observations in themselves with practical limitations on their S/N, they insert additional noise into the fitting process.

We employ a strategy intended to optimize the benefits of A0 telluric templates without any of the drawbacks (except the

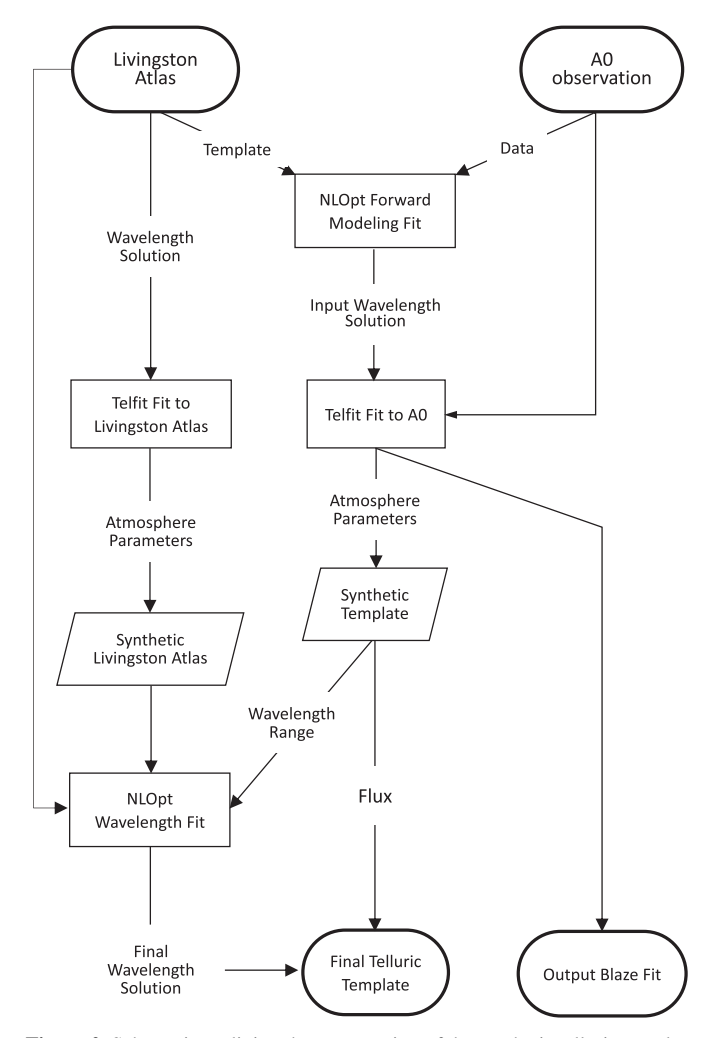


Figure 2. Schematic outlining the construction of the synthetic telluric template from the Livingston atlas and the A0 observation associated with the target data. The middle column follows the process by which the initial version of the template is produced, while the left column describes the preparation of the wavelength solution it will be combined with to produce the final template. The right column shows how the blaze fit is obtained and subsequently refined. Processes are paneled as squares, internal data products as rhomboids, and inputs/outputs as ovals.

additional observing time required). Using the Telfit (Gullikson et al. 2014) package, which is itself a python implementation of the FORTRAN Line-By-Line Radiative Transfer Model code (Clough et al. 2005), we fit the A0 spectrum associated with each target star observation to produce a high-resolution synthetic template from the best-fit parameters. Such forward modeling has been found to outperform other telluric mitigation methods, such as correction and cross-correlation (Latouf et al. 2020).

The synthetic telluric template's accuracy is essential to the performance of IGRINS RV, as it determines the reliability of the model wavelength scale and is a major factor in how well the model fits the data. The pipeline constructs the synthetic template through a series of steps, which are schematically depicted in Figure 2. The entire procedure occurs on an order-by-order basis for all specified wavelength regions and is repeated for each telluric standard associated with the target star observations. Brackett series stellar absorption does not contaminate the process, as those lines happen to coincide with

IGRINS orders that have too little telluric absorption to be used by our pipeline (Section 3.5).

First, the pipeline builds an input wavelength solution associated with the A0 spectrum that will be plugged into Telfit. This solution is provided by applying our standard NLOpt forward-modeling fit to the A0 observation, employing the Livingston atlas as a telluric template. While the Livingston atlas does not match the observed data well enough to facilitate the measurement of highly precise RVs, it is sufficient for finding an accurate wavelength solution that can then be input to Telfit. We choose to build an input wavelength solution this way as opposed to utilizing Telfit's internal wavelength solution or the wavelength solution output by the IGRINS reduction pipeline, because both of the latter are built on line information from the HITRAN database⁷ (Gordon et al. 2017). HITRANS is usually accurate to better than the m s⁻¹ level but can be discrepant by 100 m s^{-1} or more (Rothman et al. 2005), large enough to be unsuitable for this application.

Next, Telfit fits the A0 observation. By default, we only allow Telfit to vary parameters related to the abundances of the relevant molecular absorbers. For the orders used by IGRINS RV, these consist solely of CO, CH₄, and H₂O in the *K* band and CO₂, CH₄, and H₂O in the *H* band. Information on environmental conditions at the time of observation, such as the temperature and pressure, is also fed into Telfit and held fixed. Only if unknown are these allowed to vary.

IGRINS RV then takes the atmospheric parameters of the best fit and uses Telfit to generate a synthetic template comparable in resolution to the Livingston atlas. The Telfit fitting process also outputs the blaze fit, a seventh-order polynomial, which is saved separately.

In generating this synthetic spectrum, Telfit is referencing its (potentially inaccurate) internal wavelength solution. We therefore calibrate this spectrum's wavelength scale by comparing the wavelength scale of the Livingston atlas with Telfit's best fit to the Livingston atlas itself. In other words, IGRINS RV applies Telfit to the Livingston atlas as it did to the A0 observation (and over the same wavelength range), takes the atmospheric parameters of the best fit and generates a synthetic version of the atlas, and then parameterizes any difference in the output wavelength scale. It does this by using NLOpt to fit the synthetic version of the Livingston atlas to the actual atlas, with only the wavelength solution allowed to vary. This fitted wavelength scale is the final wavelength solution associated with the synthetic telluric template generated. The accuracy of the synthetic telluric template's wavelength solution is thus directly anchored to that of the Livingston atlas.

For B frames, this entire process occurs exactly as just described, but for the A frames, the synthetic telluric template is constructed slightly differently. This is because the A frame spectra exhibit a slight dip in their blaze (Section 2.2). As Telfit is only capable of modeling the blaze of a spectrum with a polynomial, its failure to account for this dip could lead to misfit absorption lines. IGRINS RV avoids this by running a spectral fit of the A frame telluric spectra (using its own spectral model) prior to applying Telfit. Because the blaze dip is properly parameterized by our spectral model, the pipeline

Table 2 Model Parameters

No.	Description
1–2	Template scale factors
3	Stellar template RV
4	Stellar $v \sin i$
5–7	Quadratic instrumental FWHM
12-14	Quadratic blaze correction
15-18	Addtl. blaze polynomial terms, as needed
19–23	Flat-field blaze correction (A frames only)

can then use the best-fit parameters for the dip to correct it out of the telluric data before they are input to Telfit.⁸

We expect the wavelength precision anchored to our telluric templates to be no greater than $10-20 \text{ m s}^{-1}$, as this is what past studies have found to be the typical RV stability of telluric lines (Seifahrt & Käufl 2008; Figueira et al. 2010).

3.4. The Model Spectrum

Our spectral model intakes a pixel scale, a blaze correction, and 18 parameters (Table 2). It begins by scaling the stellar and telluric templates through exponentiation (Table 2, Nos. 1–2) and shifting the stellar template in wavelength space by its RV offset with respect to the telluric spectrum. It then reproduces the effects of rotational broadening on the stellar template with a convolution routine and rebins both templates onto a common wavelength scale.

The templates are combined and convolved with the instrumental profile (IP), whose provenance is discussed in Section 3.6. The broadened spectrum is then binned to a cubic wavelength scale and multiplied by a model for the blaze function of the observed data. The baseline for this blaze model is a seventh-order polynomial fit to the associated telluric standard spectrum, sigma-clipped to avoid the skewing effects of absorption lines. This baseline is then combined with an optimizable polynomial (Table 2, Nos. 12–18) to account for any slight differences between the telluric standard spectrum and the target data. The set degree of this polynomial varies depending on the size of the wavelength region being fit; in some cases it is as low as two degrees and in others as high as six.

Lastly, if the spectrum is an A frame observation, a blaze correction is applied to the polynomial to account for the slight reduction in flux at the peak of the blaze (Figure 3(c)). This correction consists of a rectangular dip with a smaller, secondary rectangle descending from its rightmost edge. It is parameterized by five variables: the central location, width, and depth of the primary dip, and the width and depth of the secondary dip (Table 2, Nos. 19–23). These are allowed to vary to some extent as part of the spectral fit. Were this feature not accounted for, IGRINS RV would measure a systematic difference between A and B frame RVs.

To fit the model spectrum to the data, we used the NLOpt python package (Johnson 2008) implementation of the bound Nelder–Mead optimization algorithm (Box 1965; Nelder & Mead 1965). The optimizer starts from a set of initial parameter

 $[\]overline{{}^{7}}$ The IGRINS data reduction pipeline primarily calibrates its wavelength scales based on the OH night-sky emission lines, but in regions with no significant OH lines, such as parts of the K band, the reduction pipeline also uses line information from the HITRANS database.

This dip correction itself could be inaccurate if the Livingston atlas were used as the telluric template, because the atlas is inflexible. IGRINS RV gets around this by generating the synthetic telluric templates for all of the B frames first (before the A frames), so that the B frame synthetic templates can be used in the fitting of the A frames that characterizes the blaze dip.

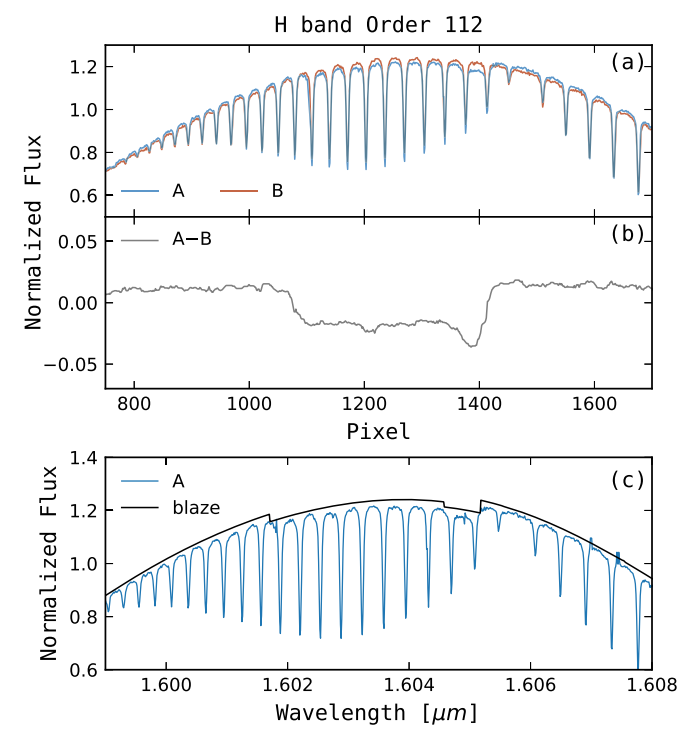


Figure 3. (a) Comparison of A and B frame spectra of an A0 standard star, zoomed in near the center of order 112 in the H band. (b) Subtracted difference between the A and B frames. The characteristic shape of the effect is evident as a rectangular dip with a smaller, secondary dip descending from the rightmost edge. Overall, the effect is proportional (increasing with detector counts), is discrete, is present in both bands, and also occurs in data taken from Gemini South. (c) IGRINS RV best-fit blaze model to the A frame spectrum, utilizing both a polynomial and the five-parameter dip model.

guesses and then moves through multiple cycles of steps, each separately fitting the blaze correction, the wavelength solution and telluric template power, the stellar template power and RV, the zeroth-order IP width, and the $v\sin i$ (when applicable). At each step, the optimizer traverses the variable parameter space and calculates the chi-squared statistic in search of a minimum. To reiterate: the wavelength solution is ultimately calibrated by synthetic telluric templates generated from A0 observations, but the solution itself is always fit for on a spectrum-by-spectrum basis for every target. The zeroth-order IP width is fit similarly, with the higher orders fixed at values determined from a large-scale analysis of A0 observations at different observatories and seasons (Section 3.6).

Barycentric velocity corrections are calculated using the astropy package (Astropy Collaboration et al. 2018) with coordinates and proper motions taken from Gaia DR2 (Gaia Collaboration et al. 2018).

3.5. Selection of Analysis Regions

Although NIR RV monitoring is best suited for a late-type star like HD 189733 (a K2 dwarf), IGRINS RV can also be effectively applied to τ Boo A (an F7 star). However, the high temperature of τ Boo A means that it exhibits little stellar content in the K band, so while both H and K bands were analyzed in the case of HD 189733, only H-band RVs were calculated for τ Boo A.

Although IGRINS covers a wavelength range 1.05 μm wide, only those echelle orders with adequate stellar and telluric absorption lines are usable by IGRINS RV. Strong stellar lines

Table 3
Selected Wavelength Regions

Order (m)	Index ^a	Wavelengths (µm)
	Н	Band
104	6	1.7206–1.7295
112	14	1.6006-1.6075
114	16	1.5690-1.5831
119	21	1.5042-1.5061, 1.5122-1.5180 ^b
120	22	1.4947–1.5065
	K 1	Band
74	3	2.3880-2.3970
75	4	2.3565-2.3697
76	5	2.3260-2.3375, 2.3418-2.3472 ^b
77	6	2.2965–2.3157, 2.3175–2.3224 ^b

Notes.

are necessary for precise RVs, and frequently spaced telluric lines are needed for an accurate wavelength solution. Through visual inspections of target star spectra, we found 10 orders in the H band (m = 100, 101, 102, 104, 111, 112, 114, 118, 119, 120) and 10 orders in the K band (m = 73, 74, 75, 76, 77, 78, 79, 81, 85, 87), each of which exhibits adequate telluric absorption. From these, we found that five orders in the <math>H band (m = 104, 112, 114, 119, 120) were well suited for Sun-like stars and six orders in the K band (m = 74, 75, 76, 77, 79, 81) were well suited for late-type stars, in terms of stellar signal. Plots of these orders are provided in Figures A1 and A2.

We selected our K-band wavelength regions by examining fits to both GJ 281 (M0) and HD 189733 (K2) spectra. By using two stars of different spectral type, $v \sin i$, and RV, observed at different air masses, we ensured that our selection is robust for a range of target star and atmospheric properties. We did the same with the H band, using HD 26257 (G2) and τ Boo A (F7) for the diagnostic fits. In total, the stars studied range from F to M dwarfs.

Beyond the requirement for well-spaced telluric and stellar absorption lines, we rejected 150 pixels on both edges of the detector to avoid poor fits resulting from the steep blaze and low S/N. We chose regions that are bookended by telluric absorption when possible, as this helps ground the cubic wavelength solution. Lastly, our visual inspections ensured that no regions are included where the stellar template is a poor fit to the data, for example, when an absorption line is present in an observation that is not in the line list of the stellar model. This last stipulation led us to reject orders 79 and 81 from the K band, leaving us with the final region selections shown in Table 3. For some regions, we also masked parts of the middle of the order that contain a dearth of stellar information (e.g., $1.506-1.510~\mu m$ in order 119 of the H band). In total, we used \sim 494 Å of spectrum in the H band and \sim 532 Å in the K band.

IGRINS RV is provided with these regions predefined, but users can also customize their own lists of wavelength regions they would like the code to fit. This may be necessary if the user is studying target stars that are outside the range of spectral types presented here. As part of Step 1, IGRINS RV will automatically take the input list of wavelength ranges and

^a The corresponding fits table layer index in IGRINS data, for user reference. ^b Orders with multiple wavelength ranges selected will fit both simultaneously, masking the intervening wavelengths to ensure that they are not included in the χ^2 goodness-of-fit calculation.

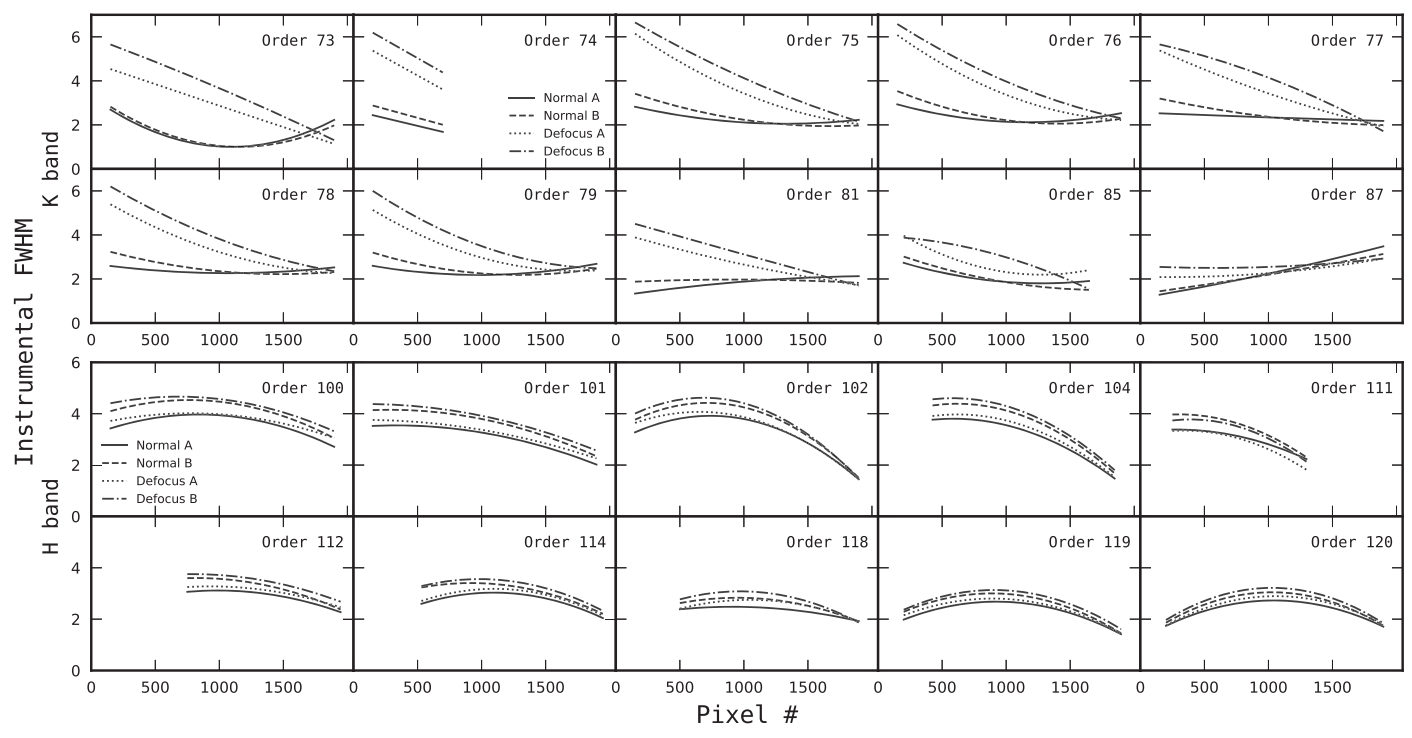


Figure 4. Fitted solutions for instrumental profile width vs. position on the detector in pixels, plotted for each echelle order with significant telluric absorption. The quadratic trend in resolution across the detector is evident, as is the diverging behavior in the *K* band for observations taken during the defocus. The trends for orders 85 and 111 are inconsistent with the others as the result of misfitting; we discard these orders from our wavelength region selection process (they feature a paucity of stellar lines regardless).

convert it into the echelle orders and pixel ranges that will be fit as part of RV estimates.

3.6. Instrumental Broadening

An accurate treatment of how resolution changes over the detector is essential for achieving the most precise RVs possible. While we found that a single Gaussian suitably models the IP at a given location within an echelle order (and the introduction of additional Gaussians leads to overfitting), the IP width can vary significantly across the detector. We employ a quadratic function in pixel space to parameterize these changes in each order. Instead of convolving narrower or wider Gaussians at each pixel location, we maintain the code's efficiency by stretching and compressing the pixel velocity scale such that convolution with a single, constant-width Gaussian produces the same results. The original pixel scale is still used for the remaining steps of producing the model spectrum.

We map the IP width variations through telluric standard fitting, which occurs as described in Section 3.3, with the important exception that now the linear and quadratic terms of the IP are allowed to vary. Each A0 star thus provides best-fit quadratics describing the IP variations across each order. We fit a total of 97 and 111 telluric standard observations in the *H* and *K* bands, respectively, with data taken over 5 yr at McD at the DCT.

Figure 4 shows the median IP fit from the ensemble of telluric standard fits, order by order, for the 10 orders with adequate telluric absorption in each of the H and K bands. Although the ensemble of fits are not pictured here for the sake of clarity, the IP curves from different observations appear largely consistent, supporting the choice of quadratics to

capture the behavior (increasing the degree of the polynomial leads only to overfitting).

The clear exceptions to this are the observations taken during the year of the *K*-band defocus. As shown in Figure 4, during this time most *K*-band orders exhibit markedly broader IP widths, corresponding to lower spectroscopic resolutions, on their shorter-wavelength parts. In *K*-band order 75, for example, the resolving power at pixel 200 decreases from roughly 53,500 to 25,000. At the higher-wavelength parts of the orders, on the other hand, the resolving power actually increases. These trends are in agreement with the behavior measured through the FWHM of sky OH emission lines (Figure 1).

We therefore undertook a separate treatment of the IP variations during this "defocus" epoch. We also modeled the IP variations for A frame observations separately from B frame observations, as the two modes of observations orient the target star differently. We found that B frame observations exhibit similar IP variations to A frames, except shifted to slightly higher IP widths; this minor difference is not unexpected given that the frames involve different positions of the target on the slit.

For each frame type, A and B, and for each time period, the "defocus" and the normal (i.e., all other times), the coefficients of these quadratics are hard-coded for use in all future fits. While the linear and quadratic terms are always held fixed at their hard-coded values, in order to take into account the possibility that different relative orientations between the star and the slit (among other things) may affect instrumental broadening, we allow the zeroth-order IP width to vary slightly during the fitting of both telluric standards and target stars.

The diverging treatment of the "defocus" time period here requires that all subsequent analysis consider observations from this period as statistically separate from those taken at other times. This has implications for estimating the pipeline's overall precision and the uncertainty of individual RV data points.

3.7. Calculating Final RVs and Uncertainties

With the completion of all the spectral fits in Step 3, IGRINS RV yields an RV value for each individual order of each observation analyzed. For each exposure, IGRINS RV calculates two statistics from the RVs of its constituent observations: the mean (RV_{ij}) and the standard deviation of the mean (σ_{ij}) , where "i" indexes different exposures and "j" indexes different orders. σ_{ij} contains information about the internal consistency of the RVs on a given night and is typically around $\sim 13~{\rm m\,s^{-1}}$ for GJ 281 and $\sim 33~{\rm m\,s^{-1}}$ for HD 26257. For a full treatment of the uncertainty, we must measure the RVs' external consistency across a longer timescale of multiple nights using RV standards.

For an RV standard star, we calculate the variance of RVs within a given order across all exposures:

$$\sigma_j^2 = \operatorname{std}(RV_{ij})^2$$
 for each order j , (1)

where "std" refers to the standard deviation. σ_j^2 thus provides information on the external RV precision of each order. However, because the scatter of RVs within an exposure also contributes to the scatter of RVs between different exposures, we must subtract out the internal uncertainty in order to determine the uncertainty in our analysis method:

$$\sigma_{\text{i(method)}}^2 = \sigma_i^2 - \text{median}((\sigma_{i,j})^2) \text{ for each order } j,$$
 (2)

where σ_j^2 is the exposure-by-exposure RV variance within an order (Equation (1)) and median($(\sigma_{i,j})^2$) is the median of the variances of the different exposures. The $\sigma_{j(\text{method})}^2$ characterizes the uncertainty in our RV measurements as the result of inadequacies of the synthetic model to ideally represent the data, the RV instability of the telluric lines being used as a wavelength calibrator, and the intrinsic RV instability of the spectral region analyzed, among other systemic factors. For GJ 281, we found σ_j to range from 38 to 55 m s⁻¹ (during the defocus, it ranged between 36 and 151 m s⁻¹), and $\sigma_{j(\text{method})}$ to typically be around 40 m s⁻¹ (85 m s⁻¹ during the defocus). For HD 26257, σ_j ranged between 78 and 241 m s⁻¹, and $\sigma_{j(\text{method})}$ was typically around 95 m s⁻¹.

Note that $\sigma_{j(method)}^2$ can only be calculated by analyzing an RV standard star, as they do not have intrinsic RV variations. An RV standard is required to estimate $\sigma_{j(method)}^2$ for each relevant echelle order in the H and K bands, as well as separately for the "defocus" epoch. These uncertainties are built into the pipeline, facilitating accurate uncertainty estimates for targets that are not RV standards. In other words, analysis of a non-RV standard would skip Equations (1) and (2), instead using the $\sigma_{j(method)}^2$ estimated from a previous analysis of an RV standard.

Using IGRINS RV in any way that significantly deviated from the form presented here (for example, deriving stellar templates from an alternate source) requires a repeat of this RV standard analysis in order to supply an estimate of $\sigma^2_{\rm j(method)}$ that accurately reflects the precision of the different method.

With a well-characterized uncertainty in the method, we can then add in a measure of the internal uncertainty for each exposure: the standard deviation of the mean of each exposure's constituent observations, σ_{ij}^2 . This provides information on uncertainties resulting from poorer-quality or more rotationally broadened data. The total RV uncertainty associated with each exposure and order is thus the quadratic sum of both uncertainties:

$$S_{ij}^2 = \sigma_{\text{j(method)}}^2 + \sigma_{ij}^2. \tag{3}$$

For each exposure, we calculate weights from S_{ij}^2 , which are then used to combine the different order RVs into one final RV and uncertainty. For each observation x,

$$w_j = \left(\frac{1}{S_{xj}^2}\right) / \left(\sum_j \frac{1}{S_{xj}^2}\right) \tag{4}$$

$$RV_{x} = \sum_{j} (w_{j} \cdot (RV_{xj} - \overline{RV_{xj}}))$$
 (5)

$$\sigma_{\mathbf{x}} = \left(\sqrt{\sum_{j} \frac{1}{\mathbf{S}_{\mathbf{x}_{j}}^{2}}}\right)^{-1}.\tag{6}$$

Each set of RVs from a given order has its mean subtracted from it before the weighted combination in Equation (5) occurs. This is because the orders have systematic RV offsets from one another (Section 4.4). The weighted mean acts linearly between orders, so the mean subtraction makes no difference for observations that have an RV estimated for all possible orders. Only for those observations that do not have an RV measurement from each order does mean subtraction change the final RV calculated.

4. Performance

The typical run time of IGRINS RV depends on the amount of memory and number of CPU cores available on the user's machine. Using an Intel Core i9-9980XE CPU with 18 cores/36 threads, a run of all 64 nights and 4 orders of GJ 281 in the K band took \sim 6.6 hr for Step 1 (Telluric Modeling) and \sim 1.2 hr for Step 3 (Analysis). As there are more orders to process in the H band, its runtimes are about 1.5 times as long.

4.1. RV Standards

We analyzed two different RV standards in order to estimate the precision delivered by IGRINS RV. Final output RVs for these targets are presented numerically in Table 4.

The results for GJ 281 are shown in Figures 5(a) and (c). The total variation over the yearlong K-band defocus is 34.2 m s⁻¹, but over the 3 yr of observations when the detector mounting was normally attached, the variation is 26.8 m s⁻¹. For the H-band analysis of HD 26257, no such distinction between epochs is necessary because only the K band was defocused, and we estimate the single precision of 46.7 m s⁻¹ across 2 yr (Figure 5(b)). We consider the 26.8 m s⁻¹ from GJ 281 to be representative of the pipeline's precision in the K band; in the next section, we demonstrate that better precision than 46.7 m s⁻¹ is achievable in the H band for narrow-line (low $V \sin i$) stars (Section 4.2).

A rare case that occurs if the corresponding data were too low quality, or there were too few observations to estimate a meaningful standard deviation, or because Telfit encountered a critical internal error when processing the night's A0 spectrum in that order.

Table 4Radial Velocity Estimates

JD -2,450,000	RV	RVerr	JD -2,450,000	RV	RVerr
(days)	(m s	-1)	(days)	(m s	⁻¹)
(1)	(2)	(3)	(1)	(2)	(3)
		GJ	281		
6984.864046	-55.18	32.95	7339.012359	-9.93	23.07
6986.015578	-1.23	25.02	7742.946759	9.01	25.79
6990.013375	-14.12	22.13	7760.922781	27.70	24.24
7334.021467	-26.22	26.51	7782.803844	3.21	26.43
7336.043078	-56.77	23.93	7799.784772	-5.48	23.76
		HD 2	26257		
7703.895107	-7.14	41.93	7760.823794	-39.53	45.74
7718.691409	41.71	45.45	7782.671744	26.80	47.85
7730.849329	33.32	42.82	7799.594995	-21.31	49.66
7742.666440	-47.86	42.41	7800.586196	22.26	47.46
7743.701591	11.62	65.34	8002.918460	-41.56	55.13
		HD 18973	33 H Band		
7145.832605	19.49	45.03	7296.710870	-70.17	46.94
7145.853588	-25.14	47.89	7296.715998	-62.02	47.38
7145.907048	-15.97	51.53	7296.721085	-67.35	47.99
7292.688153	-242.44	44.41	7511.834885	16.08	42.28
7296.705488	-30.19	46.00	7511.848233	-16.43	42.55
		HD 18973	33 K Band		
7145.832605	28.15	28.27	7296.710870	3.01	22.49
7145.853588	-34.69	25.76	7296.715998	-8.94	24.42
7145.907048	-67.53	33.72	7296.721085	1.27	22.67
7292.688153	-158.41	22.99	7511.834885	21.75	21.87
7296.705488	33.18	25.27	7511.848233	19.95	21.99
		au Bo	оо А		
7029.929227	282.70	43.09	7049.965269	74.26	46.87
7029.934594	206.34	45.12	7049.969094	96.48	44.27
7029.991209	216.24	44.65	7049.973087	115.17	45.48
7049.957766	110.33	57.15	7049.976898	93.84	44.67
7049.961611	118.57	44.05	7050.030828	57.04	46.46

(This table is available in its entirety in machine-readable form.)

The uncertainty in each target's individual RVs agrees well with the overall RV variation measured. The average uncertainty of the GJ 281 RVs is 26.5 m s^{-1} , and the average uncertainty of HD 26257's RVs is 46.8 m s^{-1} .

IGRINS RV also estimates the $v \sin i$ of the target star from its spectral model fits and converts these values into a single, final $v \sin i$ measurement. The procedure is almost exactly the same as used for determining an average final absolute RV (Section 4.4).

We estimate a $v \sin i$ of 2.96 ± 0.31 km s⁻¹ for GJ 281. This appears to be in rough agreement with the literature. Schöfer et al. (2019) measured the $v \sin i$ to be 2 km s⁻¹, while Hojjatpanah et al. (2019) placed an upper limit on the $v \sin i$ of 2 km s⁻¹, but these values cannot be strictly compared with our own because they do not have uncertainties associated with them. Likewise, though our $v \sin i$ measurement of 9.24 ± 0.15 km s⁻¹ for HD 26257 may be somewhat overestimated compared to the literature values of 7.2 km s⁻¹ (Głębocki & Gnaciński 2005) and 5.3 km s⁻¹ (Brewer et al. 2016), neither of the last two is reported with uncertainties.

There is some reason to expect IGRINS RV to have trouble determining $v \sin i$ in certain cases. The instrumental profile that IGRINS convolves with the stellar rotational profile is ~ 7 km s⁻¹ wide (Mace et al. 2016b); for stars with rotational broadening much narrower than this, it may be difficult to measure $v \sin i$ accurately.

Figures 6(c) and (d) show the $v \sin i$ results for GJ 281 and HD 26257 for a run of Step 3 where $v \sin i$ is allowed to vary. We observe that GJ 281's $v \sin i$ estimates became significantly less precise and less accurate during the K-band defocus, when the instrumental profile was much wider in some regions. Order 74 is a particularly good example. The analysis region of this order covers the part of the detector in which the resolution change manifested as a severe decay (Figure 4). As a result, the IGRINS RV pipeline was not able to detect any of the rotational broadening of GJ 281, often measuring a $v \sin i$ of 0 km s⁻¹. The code is configured to automatically discard $v \sin i$ estimates from order 74 for observations taken during the defocus epoch.

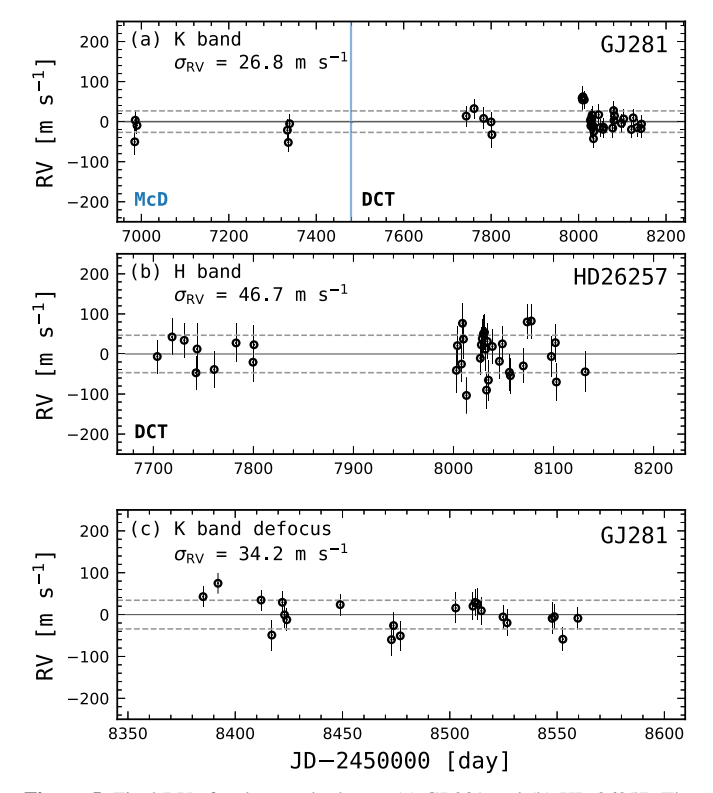


Figure 5. Final RVs for the standard stars (a) GJ 281 and (b) HD 26257. The GJ 281 observations span both McD and Lowell Observatory data, as well as data taken during the K-band defocus. Dashed lines indicate 1σ deviations from the mean.

Final runs of target stars should always fix $v \sin i$ at a constant value, given that the physical property presumably remains constant over the time frame of the observations. The inaccuracy of IGRINS RV in estimating the $v \sin i$ of target stars can thus be expected to introduce some level of imprecision in the RVs. To test this, we executed a run of Step 3 for each of our target stars in which $v \sin i$ was allowed to vary, providing an estimate of its value and an uncertainty in that estimate. We then ran Step 3 three times: once with $v \sin i$ held fixed at this value, and once on a subset of nights with $v \sin i$ held fixed at this value plus 1σ and minus 1σ . We find an average absolute difference in RV of <1 m s⁻¹. We do not find any sign of higher $v \sin i$ inputs corresponding to higher RV outputs, or vice versa.

We caution users to perform this exercise for all target stars with high (>10 km s^{-1}) $v \sin i$ and/or those for which they require the most strictly accurate RV uncertainty estimates. Because the effect of $v \sin i$ on RVs appears uncorrelated, only one additional run with $v \sin i$ fixed at either 1σ greater or 1σ less than its estimated value will appropriately gauge the additional uncertainty term introduced as the standard deviation of the difference in RVs between the two runs. This additional uncertainty term is typically around 2–5 m s⁻¹, except for in the case of τ Boo A, where it can be as high as \sim 9 m s⁻¹ (to be expected, given the higher $v \sin i$ of τ Boo A). The new uncertainty can then be added in quadrature with the preexisting RV uncertainties, and an additional code module, Step 4, is provided as part of IGRINS RV to automate this calculation.

All RVs presented in this paper have had their uncertainties determined with this method.

4.2. Validation of Planetary Systems

While monitoring RV standard stars allows a determination of IGRINS RV's precision, only the recovery of an established stellar RV signal can test the code's reliability. We applied IGRINS RV to two stars with well-characterized planetary companions: HD 189733 and τ Boo A.

Output RVs are presented in Figure 7, with numerical values available in Table 4. Both stars exhibit RV dispersions much greater than the typical uncertainties in their measurements: $360.0~{\rm m~s^{-1}}$ versus $46.9~{\rm m~s^{-1}}$ for τ Boo A, $167.3~{\rm m~s^{-1}}$ versus $43.1~{\rm m~s^{-1}}$ for HD 189733 in the H band, and $158.4~{\rm m~s^{-1}}$ versus $23.1~{\rm m~s^{-1}}$ for HD 189733 in the K band. This indicated possible planet-induced reflex motion was occurring.

For each target, we searched for periodicity using the astropy (Astropy Collaboration et al. 2018) implementation of Lomb-Scargle periodograms and then obtained an orbital fit using exoplanet (Foreman-Mackey et al. 2020) in combination with a maximum likelihood optimization routine. The best-fit parameters became the starting point of a Markov Chain Monte Carlo analysis, which we implemented with the PyMC3 (Salvatier et al. 2016) tool. ¹⁰ Four walkers were used, each with at least 20,000 steps and with the first 10,000 steps as burn-in.

The planet-induced RV signals were recovered in both the H- and K-band data for HD 189733, as well as in the H-band data for τ Boo A. Orbital fits are displayed in Figures 8 and 9. All Keplerian fit parameters are in agreement with published values (Table 5).

The fit to our measured RVs for τ Boo A was slightly complicated by the presence of the companion τ Boo B. Proceeding based off of Figure 3 of Justesen & Albrecht (2019) (the processed RVs were unavailable), we represented the M-dwarf companion's influence through a linear RV trend, which we fit for in combination with the planet-induced RV model. The result indicates that τ Boo B produced a -149.63 ± 6.03 m s⁻¹ yr⁻¹ slope (Figure 9, top panel) in the RV of τ Boo A over the course of our observations. This slope is comparable to the \sim -100 m s⁻¹ yr⁻¹ RV slope we estimate from Justesen & Albrecht (2019).

Nearly one-third of our RV measurements for HD 189733 were taken during transit, and we indeed observe deviations in these RVs consistent with the Rossiter–McLaughlin effect (Figures 8(a) and (b)). The semiamplitude, $\sim 50 \text{ m s}^{-1}$, and the duration of the effect, ~ 0.08 days, appear consistent with those of Moutou et al. (2020) in their NIR observations of HD 189733 with SPIRou (displayed in their Figure 4).

We did not analyze HD 189733 with the intention of observing the Rossiter–McLaughlin effect, and we consider its unexpected detection in our measured RVs to be further confirmation of the accuracy of the IGRINS RV code. Additionally, this indicates that the true scatter of the orbital fit residuals for HD 189733 is likely smaller than measured, as Moutou et al. (2020) found that including the Rossiter–McLaughlin effect in their model during MCMC fitting reduced the scatter of their residuals by an average of 34%.

The scatter of the orbital fit residuals compares favorably with that of the RV standards, while also tracing the effects of $v \sin i$ on precision. In the K band, the residuals for HD 189733, 23.2 m s⁻¹, exhibited similar scatter to what we saw in the RV standard GJ 281, 26.8 m s⁻¹. Both stars have a comparably

¹⁰ The orbital fit was done following the steps described at https://docs.exoplanet.codes/en/stable/tutorials/intro-to-pymc3/.

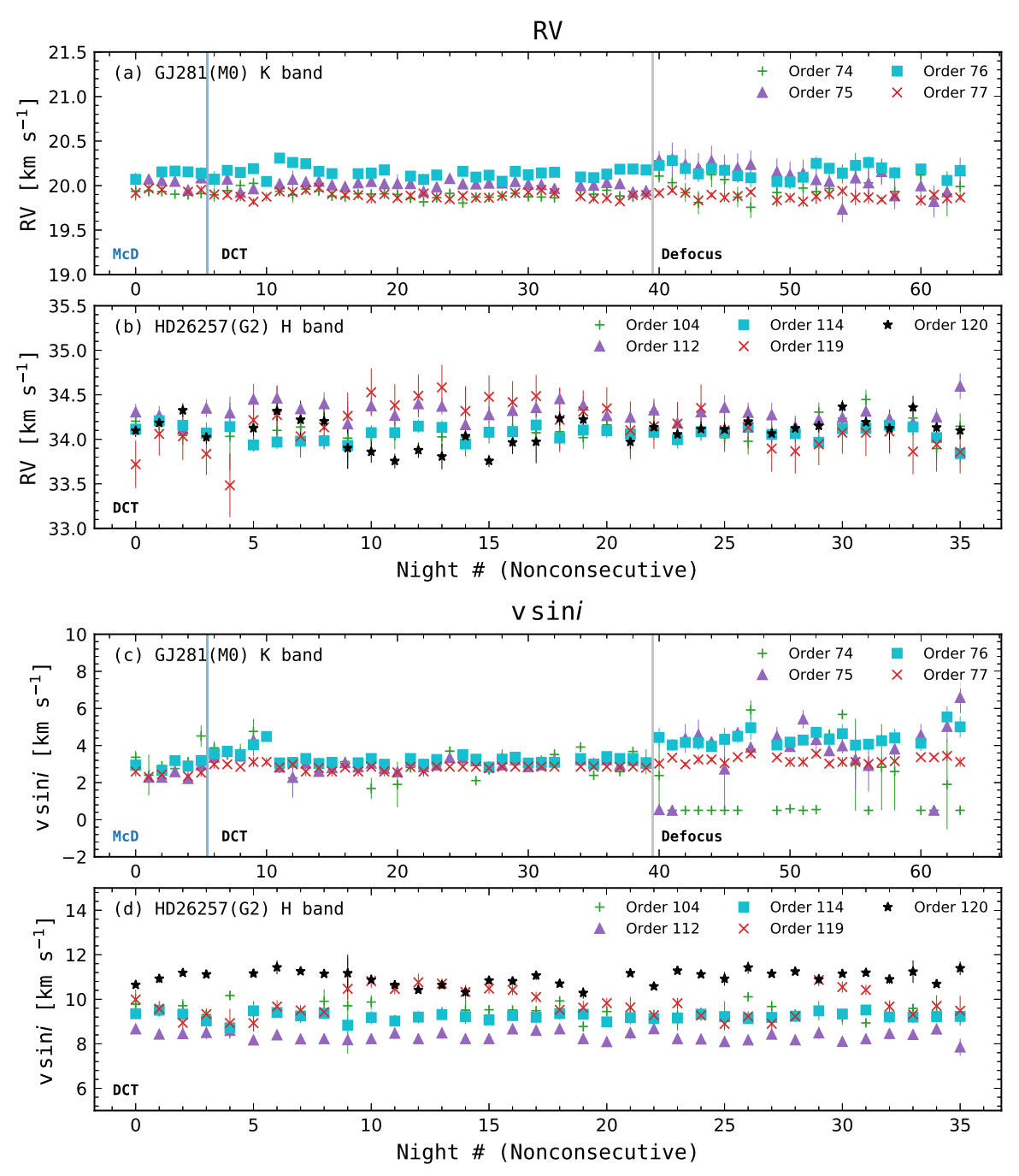


Figure 6. Top panels: RVs for the standard stars (a) GJ 281 and (b) HD 26257 separated by order. Error bars are computed as the quadratic sum of the method uncertainty and the RV scatter within an exposure. Bottom panels: $v \sin i$ measurements separated by order for GJ 281 (c) and HD 26257 (d). Vertical axes have equal scaling for ease of comparison.

small $v \sin i$ of 2–4 km s⁻¹. In the H band, the standard deviation of the HD 189733 orbital fit residuals was 31.1 m s⁻¹, smaller than the precision obtained from the RV standard HD 26257, 46.7 m s⁻¹. This is explained by the faster rotation of HD 26257 ($v \sin i \sim 10$ km s⁻¹) compared to HD 189733 ($v \sin i \sim 4$ km s⁻¹). The stronger rotational broadening produces shallower stellar absorption lines, which in turn is associated with lower RV information content (Butler et al. 1996).

This trend is also seen in τ Boo A, which has an even higher $v \sin i$ of $\sim 20 \text{ km s}^{-1}$ and delivers a standard deviation around its orbital fit of 56.28 m s⁻¹. This target was highly saturated in

the IGRINS slit-viewing camera during observations, making it difficult to center the star in the slit and ensure that it was in the same place for every observation. It is therefore possible that a changing slope in the slit illumination resulting from guiding and/or centering variations might have contributed to this higher error, not just the $v \sin i$.

Taken as a whole, these results suggest that the true baseline precision IGRINS RV is capable of in the H band is actually 31.1 m s⁻¹, as opposed to 46.7 m s⁻¹, for stars with relatively low $v \sin i$ ($\lesssim 5 \text{ km s}^{-1}$).

The fact that the precision changes with $v \sin i$ does not mean that IGRINS RV underestimates its output RV uncertainties. If

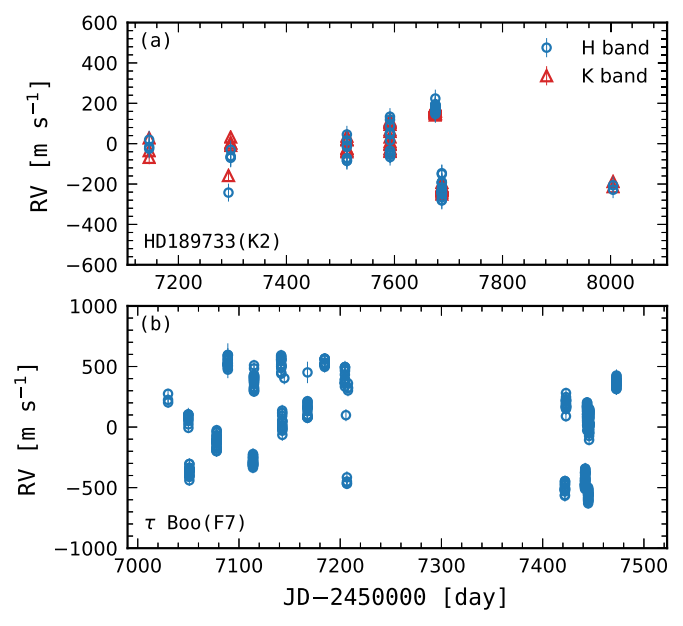


Figure 7. RVs for (a) HD 189733 and (b) τ Boo A.

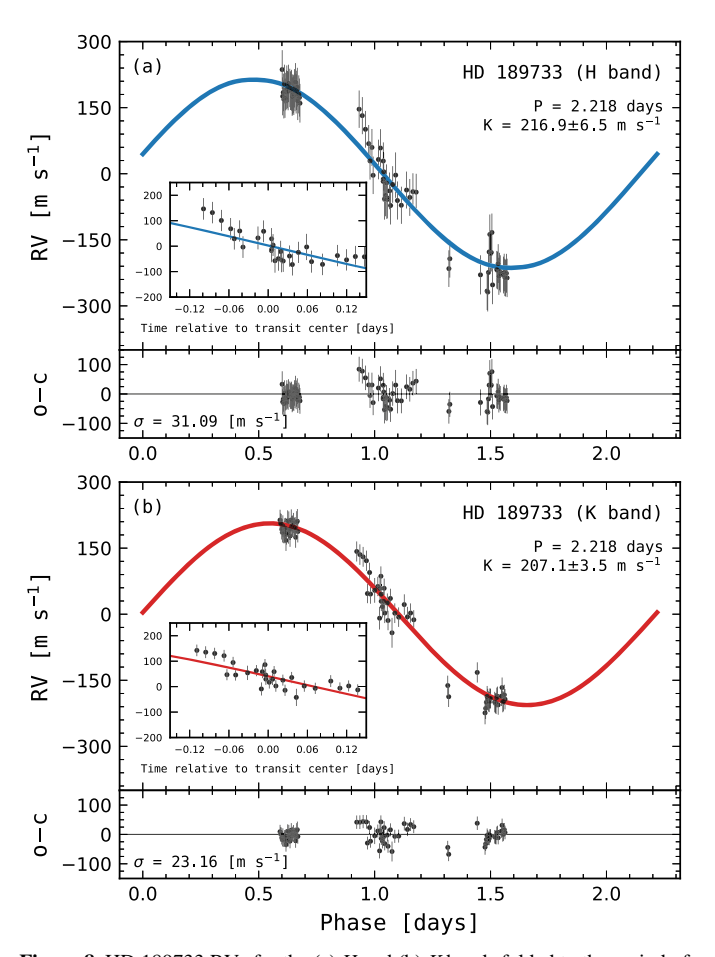


Figure 8. HD 189733 RVs for the (a) H and (b) K bands folded to the period of best fit. Transparent lines indicate the MCMC orbital fit; residuals from the mean fit are shown beneath.

a spectrum contains less RV information content, this will be reflected in a higher scatter for the RVs calculated from different exposures within an observation, producing final RV uncertainties that are appropriately higher as well. This

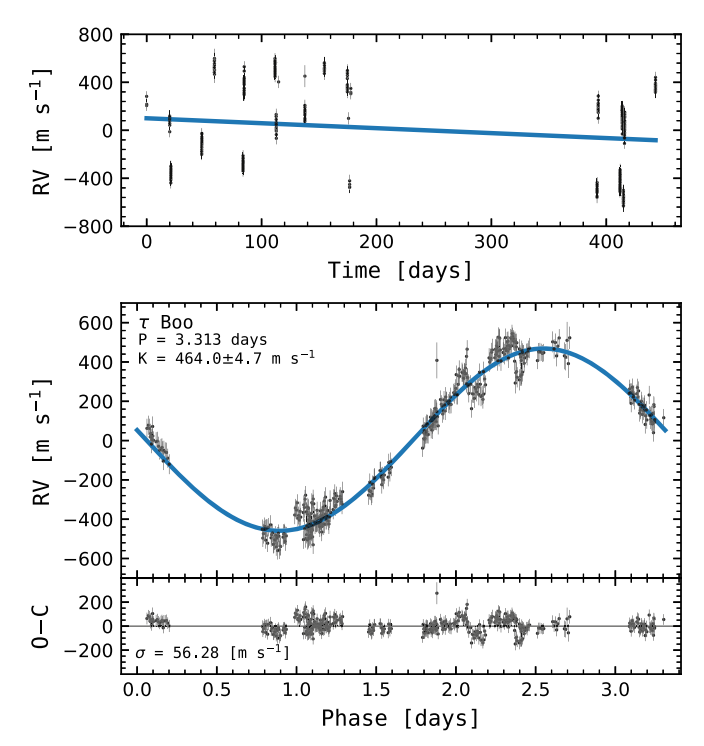


Figure 9. Top panel: τ Boo A H-band RVs alongside the best fit for the trend induced by the M-dwarf companion. Bottom panel: same RVs folded to the period of best fit, with the line indicating the mean MCMC orbital fit, and with residuals from the mean fit shown beneath.

Table 5Keplerian Fit Parameters

	proman i it i urumotore	
	This Study	Literature
]	HD 189733 H Band	
Period (days)	2.218	2.219 ± 0.0005
Orbital eccentricity	0.0028 [fixed] ^a	0 [fixed]
RV semiamplitude (m s ⁻¹)	216.86 ± 6.55	205 ± 6
1	HD 189733 K Band	
Period (days)	2.218	2.219 ± 0.0005
Orbital eccentricity	0.0028 [fixed] ^a	0 [fixed]
RV semiamplitude (m s ⁻¹)	207.21 ± 3.54	205 ± 6
	au Boo	
Period (days)	3.313	3.3124568 ± 0.0000069
Orbital eccentricity	0.014 ± 0.008	0.011 ± 0.006
RV semiamplitude (m s ⁻¹)	464.02 ± 4.68	471.73 ± 2.97
RV trend (m s ⁻¹ yr ⁻¹)	-150.82 ± 6.07	

Notes. Literature values for HD 189733 and τ Boo are from Bouchy et al. (2005) and Borsa et al. (2015), respectively.

behavior is discernible in the RVs of the planet hosts, where the uncertainties increase proportionally to the scatter around the true RV signal such that $>1\sigma$ outliers appear less than 32% of the time, while $>2\sigma$ outliers occur less than 5% of the time.

4.3. Template Choice

As shown in Figures 10(a) and (c), moderate (\sim 400 K) mismatches in $T_{\rm eff}$ between the chosen stellar template and the

^a From transit data (Ballard 2019). Uncertainties on periods from this study are negligibly small.

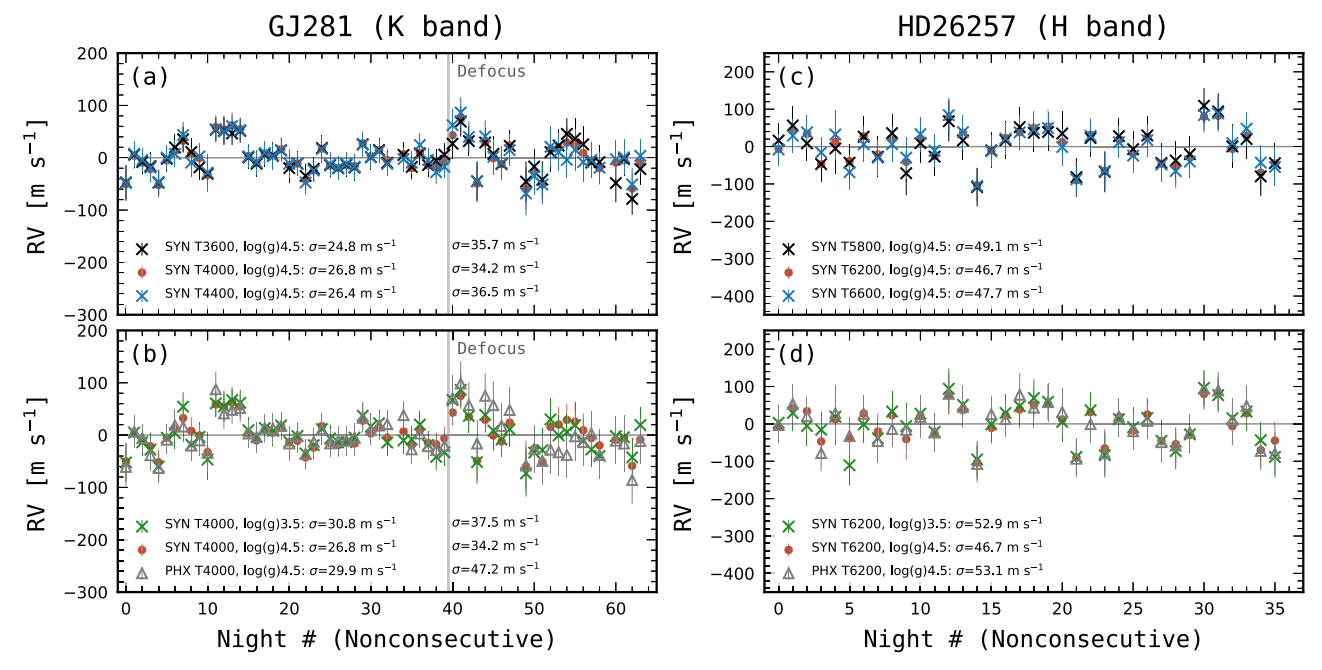


Figure 10. RVs for the standard stars GJ 281 and HD 26257 using stellar templates with different effective temperatures (panels (a) and (c)) and log *g* (panels (b) and (d)). Panels (b) and (d) also display results calculated with a template constructed with the same stellar parameters but different software. SYN refers to our synthetic stellar templates produced with VALD and PHOENIX NextGen, and PHX refers to stellar templates from the Göttingen Spectral Library (Husser et al. 2013).

target star have little effect on the IGRINS RV results. For GJ 281 and HD 26257, such template changes amount to only a few m s⁻¹ difference in precision at most. Mismatches in $\log g$ appear to have similarly small effects (Figures 10(b) and (d)). In addition, we tested IGRINS RV with stellar templates from the Göttingen Spectral Library¹¹ (Figures 10(b) and (d); Husser et al. 2013).

Unlike with $v\sin i$ or average RV, IGRINS RV does not come with any built-in functionality to converge to more accurate stellar template parameters. The only way for the user to check their choice of stellar template is to run Step 2 or 3 with stellar templates of different parameters and compare their output uncertainties and model fit plots.

When selecting a stellar template, the more closely the stellar template resembles the target star, the more precise the results will be. To some extent, worse spectral fits resulting from a less accurate stellar template will be reflected in a higher scatter for the RVs calculated from different exposures within an observation, meaning that the final RV uncertainty estimates will be appropriately higher as well.

However, if using stellar templates produced by a means other than the one presented here, there is no guarantee that the mismatch behavior will fully encapsulate the intra-exposure uncertainty introduced. Only another analysis of an RV standard would provide a robust quantification of the precision of the code in this context. For instance, Figures 10(b) and (d) show that running our RV standards with synthetic stellar templates produced with a different model atmosphere code and line list (Husser et al. 2013) results in lower precision. In the K band, the increased scatter occurs in tandem with increased intra-exposure uncertainty (the error bars), but in the H band it does not, such that the full internight scatter only calculable from an RV standard is required for an accurate characterization of the precision.

4.4. Absolute RVs

IGRINS RV can also deliver absolute—as opposed to relative—RVs. The absolute RVs measured from different orders are usually consistent with each other within uncertainties, as are the means of the RVs from each order (Figures 6(a) and (b)). However, on occasion one or more orders exhibit zero-point offsets in RVs from the rest (e.g., order 76 in the GJ 281 analysis). These relative offsets between orders are consistent for a given target, but not between targets. The behavior persists to some extent in all observations, and in some cases the discrepancies are larger than those shown here.

A wide array of diagnostic tests were undertaken to determine whether these offsets were caused by an inadequate treatment of true variations between echelle orders in the spectra. Ultimately, we found that the effect is inconsistent with a systematic origin, such as a wavelength calibration error or an error in instrumental profile modeling, and is instead best explained by slight inaccuracies in the depths and/or wavelengths predicted for the absorption lines in either our stellar models, telluric models, or both. Future versions of IGRINS RV will explore means of reducing such discrepancies.

As the effect only influences the zero-point offsets of the RVs derived from each echelle order, it can be mitigated in a relatively straightforward manner. Although a more involved correction could be applied, such as the Trend Filtering Algorithm used in Cale et al. (2018) to detrend order-dependent RVs, we found that subtraction of the mean RV from each order before weighted combination (Equation (5)) successfully mitigated the effect without introducing the risk of overfitting our results. Because the relative RV variations are precise, the pipeline's capabilities when it comes to RV monitoring experiments and planet detection are unaffected.

IGRINS RV still provides the ability to compute absolute RVs. In this setting, the discrepancy between the RV zeropoints of different orders is treated as a source of uncertainty in

¹¹ http://phoenix.astro.physik.uni-goettingen.de/?page_id=15 These spectra require flattening before use.

itself, which is added into the final RV uncertainties. In some cases, this added uncertainty will be small, and the precision of absolute RV measurements will be comparable to those reported here for relative RVs, but this is not guaranteed. The absolute RV is therefore provided in support of science cases other than planet detection, in which km s⁻¹ characterization of an absolute RV is all that is required (e.g., star cluster and moving group member identification and star cluster dynamic studies; Tang et al. 2019; Pang et al. 2020, 2021). The absolute RV's IGRINS RV derived for our RV standards (Table 1) exhibited slightly less precision, with mean RV uncertainty increasing to $30-45 \text{ m s}^{-1}$ for GJ 281 and 53 m s⁻¹ for HD 26257. Both of these RVs were relatively accurate as well: we found the absolute RV of GJ 281 in both the normal and defocused epochs to be within the uncertainties of the value provided by Maldonado et al. (2010), $20.23 \pm 0.26 \,\mathrm{km \, s}^{-1}$. For HD 26257, although the pipeline's absolute RV disagrees with the value of $33.649 \pm 0.0055 \,\mathrm{km \, s^{-1}}$ reported by Soubiran et al. (2018), the discrepancy is only 0.267 km s^{-1} . This suggests that IGRINS RV delivers absolute RVs good to a systematic uncertainty of a few hundred meters per second.

4.5. Suggested Observing Strategy

To optimize RVs calculated from IGRINS observations, telluric standard observations are a requirement and should be taken immediately before or after science target observations (and within ~ 0.3 in air mass). Telluric standards observed at more discrepant air masses can still be used, albeit with caution. If the characteristics of the atmosphere remained the same between the standard and science target observations, then the spectral model's ability to adjust the telluric template's power should adequately compensate for a relatively significant difference in air mass. However, if the atmosphere changed significantly over the course of the night (e.g., humidity increased), then the telluric template generated from the standard may poorly correspond to the absorption featured in the science target spectra. This would result in model misfits and, potentially, poor RVs. If users use telluric standards at discrepant air masses, we suggest that they refer to the relevant weather logs and check the fit plots outputted by IGRINS RV for the observation(s) in question.

As the atmosphere can be highly variable from night to night, we discourage trying to substitute telluric standard observations from different nights. Other than telluric standards, there is no need to take additional calibrations beyond what is required for typical IGRINS observing.

If the user is constructing stellar templates following a different procedure than that presented here, employing alternate wavelength regions for analysis, or otherwise altering the pipeline in ways that would systematically affect its performance, observations of an RV standard star are required to characterize the precision of the alternate method. We suggest that RV standards be narrow-line stars observed repeatedly across multiple epochs.

Lastly, we recommend that users observe in a nodding sequence of at least four frames (i.e., ABBA as opposed to AB). This allows for better characterization of the internal RV uncertainty within a given night of observation. If users are unsure what exposure time will yield their desired S/N, we recommend first taking one AB pair and measuring its S/N on the fly. The user can then decide whether they need to take only one more AB pair or to adjust the exposure time and take two.

5. Summary and Future Prospects

We present IGRINS RV, an open-source python pipeline for computing RV measurements from reduced IGRINS spectra. Although IGRINS was not designed to produce precise RVs, by applying a modified forward-modeling technique to the cross-dispersed echelle spectrograph format, we find that the wide wavelength range of IGRINS allows us to achieve high-precision measurements.

With this large wavelength range—the full H and K bands—comes a variety of challenges. Instrumental profile variations across the detector are significant and require extensive modeling, especially given a yearlong period when the K band was defocused. Furthermore, a large portion of the H and K bands have inadequate information content to deliver accurate RVs, such that the regions used by IGRINS RV had to be handpicked based on a variety of criteria. We ultimately found a total of \sim 494 Å in the H band suitable for the analysis of an F7 star, a G2 star, and a K2 star (τ Boo A, HD 26257, and HD 189733, respectively); \sim 532 Å in the K band were used in the analysis of an M0 star and a K2 star (GJ 281 and HD 189733).

Perhaps most importantly, telluric absorption is extremely variable, and static templates are not viable over these large wavelength ranges. Instead, we use a combination of Telfit and our own forward-modeling code to construct accurate, high-resolution telluric templates on a night-by-night basis. This provides a common-path wavelength calibrator while also alleviating the need to mask or correct for telluric lines.

IGRINS RV requires no additional instrument hardware, such as a gas cell or laser frequency comb. Only accompanying observations of telluric standard stars are a prerequisite.

The IGRINS RV pipeline succeeds in achieving nearly 10 times better precision than the method previously applied to measure RVs with IGRINS (Mace et al. 2016b), demonstrating a precision in the K band of 26.8 m s⁻¹ when applied to the narrow-line star GJ 281 ($v \sin i \sim 3 \text{ km s}^{-1}$) and 31.1 m s⁻¹ in the H band when applied to HD 189733 ($v \sin i \sim 4 \text{ km s}^{-1}$). These precisions are validated by a monitoring campaign of RV standard stars and the successful retrieval of the planet-induced RV signals of HD 189733 and τ Boo A from actual observational data.

IGRINS RV has been tested successfully with Gemini South data. Though its performance on Gemini South observations has not been characterized with an RV standard, we expect the capabilities reported here to extend to such data. The RVs (Figures 6(a) and (b)), stellar rotational velocities (Figures 6(c) and (d)), and instrumental profile patterns (Figure 4) all appear consistent in accuracy and precision between observations taken at McD and DCT. Observations taken from Gemini South may actually produce better-quality RVs than those presented here, as the smaller slit (0.1934) may reduce variations in slit illumination.

Future versions of <code>IGRINS RV</code> will explore means to further improve the accuracy of our stellar and telluric models in order to reduce the zero-point RV discrepancies measured between echelle orders. Additionally, a new version of <code>IGRINS RV</code> will be released once the <code>IGRINS</code> plp is updated to address the flux suppression effect observed in reduced A frames.

IGRINS RV comes with a high degree of built-in functionality and is designed for ease of use. The software can be run entirely from the command line, and should the user choose to modify it in any way, the code is extensively

commented. For full instructions on how to run IGRINS RV, a detailed instruction manual is available on the wiki page at the GitHub repository (Tang et al. 2021, submitted).

NIR RVs provide a valuable tool for planet detection around spotted and active stars, especially T Tauri stars, because the lower impact of stellar activity at longer wavelengths can distinguish between apparent RV variation arising from cool spots and planetary companions. At the same time, M dwarfs, important targets for exoplanet searches (France et al. 2016), yield the best S/N in the NIR because they emit most of their light at longer wavelengths. The IGRINS RV pipeline facilitates this valuable application for an already powerful spectrograph. Moreover, our code provides a proof of concept for a precise RV methodology that can be developed for other NIR echelle spectrographs not necessarily designed for such experiments.

We are grateful to the anonymous referee for a timely, constructive, and insightful report that improved the quality and presentation of our manuscript. We thank the technical and logistical staff at McDonald and Lowell Observatories for their excellent support of the Immersion Grating Infrared Spectrograph (IGRINS) installations, software, and observation program described here, in particular, D. Doss, C. Gibson, J. Kuehne, K. Meyer, B. Hardesty, F. Cornelius, M. Sweaton, J. Gehring, S. Zoonematkermani, E. Dunham, S. Levine, H. Roe, W. DeGroff, G. Jacoby, T. Pugh, A. Hayslip, and H. Larson. We also thank Laura Flagg for her insightful conversations. Partial support for this work was provided by NASA Exoplanet Research Program grant 80-NSSC19K-0289 to L.P. C.M.J.-K. would like to acknowledge partial support for this work provided through grants to Rice University provided by NASA (award 80-NSSC18K-0828) and the NSF (awards AST-2009197 and AST-1461918). We are grateful for the generous donations of John and Ginger Giovale, the BF Foundation, and others that made the IGRINS-DCT program possible. Additional funding for IGRINS at the DCT was provided by the Mt. Cuba Astronomical Foundation and the Orr Family Foundation. IGRINS was developed under a collaboration between the

University of Texas at Austin and the Korea Astronomy and Space Science Institute (KASI) with the financial support of the US National Science Foundation under grants AST-1229522 and AST-1702267, of the University of Texas at Austin, and of the Korean GMT Project of KASI.

This work has made use of the VALD database, operated at Uppsala University, the Institute of Astronomy RAS in Moscow, and the University of Vienna. This study also made use of the SIMBAD database and the VizieR catalog access tool, both operated at CDS, Strasbourg, France. These results made use of the Lowell Discovery Telescope (LDT) at Lowell Observatory. Lowell is a private, nonprofit institution dedicated to astrophysical research and public appreciation of astronomy and operates the LDT in partnership with Boston University, the University of Maryland, the University of Toledo, Northern Arizona University, and Yale University. We have used IGRINS archival data older than the 2 yr proprietary period.

Facilities: Lowell Discovery Telescope (LDT, formerly the Discovery Channel Telescope, DCT), McDonald Observatory (McD).

Software: astropy (Astropy Collaboration et al. 2018), exoplanet (Foreman-Mackey et al. 2020), pymc3 (Salvatier et al. 2016), theano (Theano Development Team et al. 2016), The IvS Python Repository (Institute for Astronomy at KU Leuven 2018), BMC (Duarte & Watanabe 2018), Telfit (Gullikson et al. 2014), NLOpt (Johnson 2008).

Appendix A Spectra Plots for RV Standards

The IGRINS spectrograph splits the H and K bands into 28 and 26 echelle orders, respectively. From these orders, we selected only a handful of wavelength regions for analysis. Our criteria are described in Section 3.5; here, we illustrate the results of their application with example spectra of GJ 281 (Figure A1) and HD 26257 (Figure A2) across six orders in the K band and H band, respectively. Only the first four of K band orders depicted ultimately made our cuts.

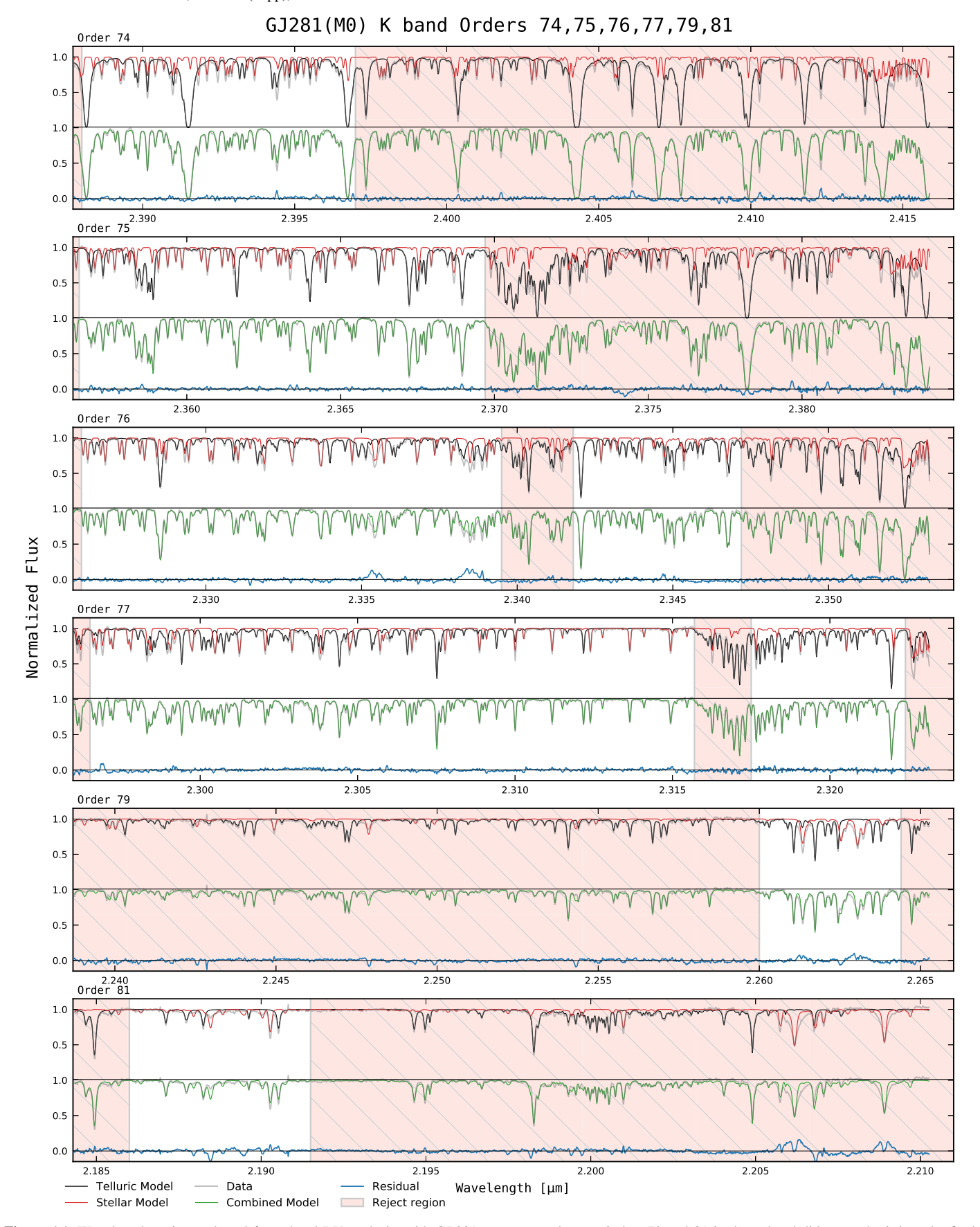


Figure A1. Wavelength regions selected for *K*-band RV analysis, with GJ 281 as an example star. Orders 79 and 81 in the *K* band did not make it into the final selection, as they only exhibited small regions of significant, interspersed stellar and telluric absorption. Crossed-out regions were rejected or masked based on the criteria listed in Section 3.5, with the exception of the large area of order 74 that was rejected because of improper telluric fitting. The regions displayed were trimmed by 150 pixels on each side to remove the worst of the blaze effects.

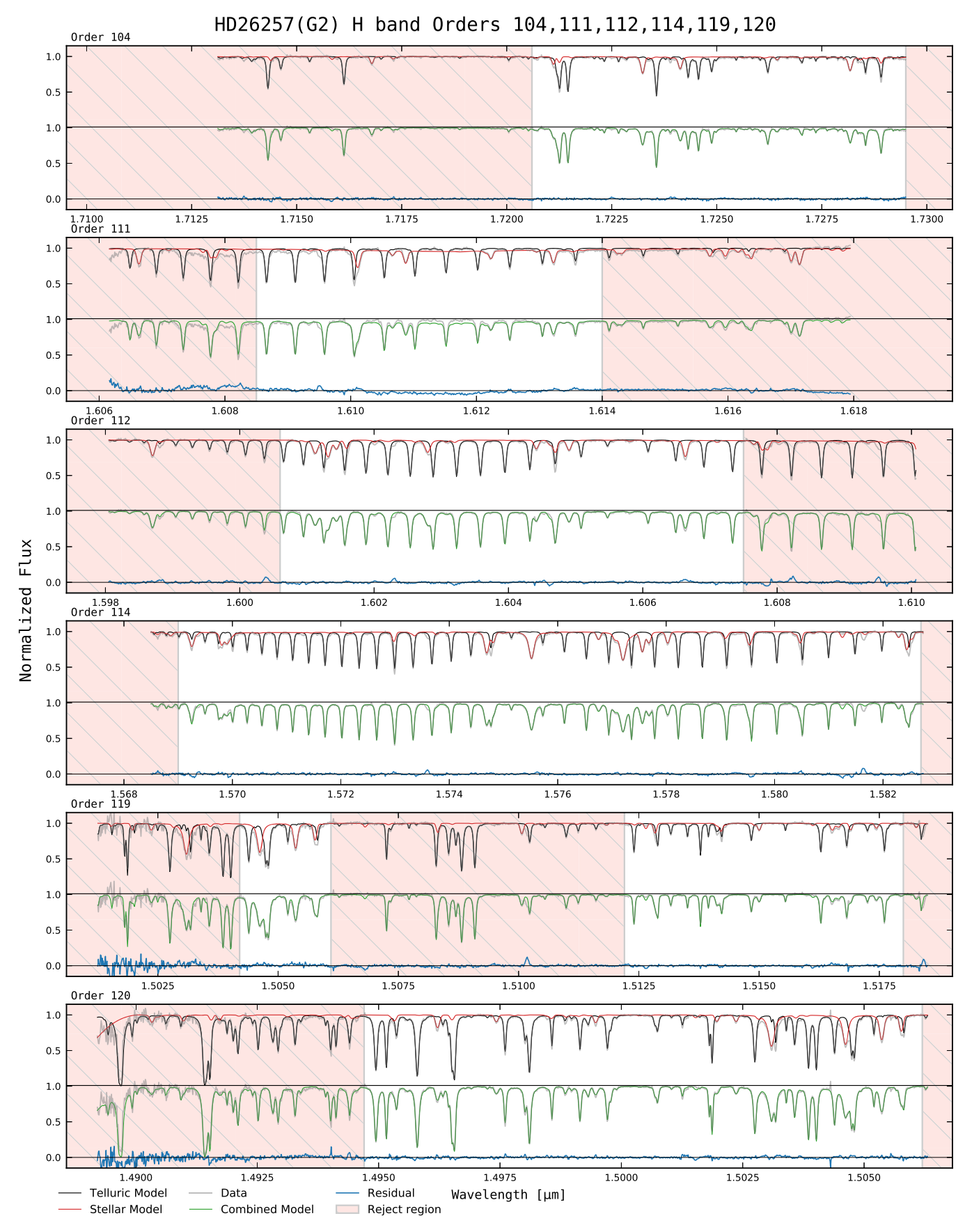


Figure A2. Final sample of wavelength regions selected for H-band RV analysis, with HD 26257 as an example star.

Appendix B Observation information for Science Targets

In this Appendix, we provide details on the IGRINS observations used to demonstrate the performance of the IGRINS RV pipeline. Table B1 lists our observations of the

RV standard stars GJ 281 and HD 26257, Table B2 lists our observations of the known planet hosts $\tau \, \text{Boo} \, \text{A}$ and HD 189733, and Table B3 summarizes the telluric standard stars that were observed in accompaniment with the RV standards and known planet hosts.

Table B1IGRINS Observations for RV Standards

UT Date	S/N ^a	Nod Seq.	AM	Facility	UT Date	S/N ^a	Nod Seq.	AM	Facility	UT Date	S/Nª	Nod Seq.	AM	Facility
(yyyymmdd) (1)	(2)	(3)	(4)	(5)	(yyyymmdd) (1)	(2)	(3)	(4)	(5)	(yyyymmdd) (1)	(2)	(3)	(4)	(5)
						GJ	281 (K Band)							
20141122	55	ABBA	1.26	McD	20171005	109	AB	1.28	DCT	20181019	119	AB	1.19	DCT
20141123	95	ABBA	1.31	McD	20171006	97	AB	1.46	DCT	20181024	89	ABBA	1.19	DCT
20141127	150	ABBA	1.35	McD	20171007	128	AB	1.27	DCT	20181029	110	AB	1.25	DCT
20151106	132	ABBA	1.18	McD	20171018	126	AB	1.20	DCT	20181030	79	ABAB	1.20	DCT
20151108	129	AB	1.25	McD	20171021	147	AB	1.19	DCT	20181031	181	AB	1.19	DCT
20151111	135	ABBA	1.19	McD	20171028	162	AB	1.19	DCT	20181125	124	ABBA	1.19	DCT
20161219	72	ABAB	1.29	DCT	20171029	124	AB	1.44	DCT	20181219	111	AB	1.33	DCT
20170106	114	AB	1.40	DCT	20171119	89	AB	1.19	DCT	20181220	161	AB	1.42	DCT
20170128	91	AB	1.21	DCT	20171121	136	AB	1.38	DCT	20181223	141	AB	1.25	DCT
20170214	185	AB	1.27	DCT	20171122	185	AB	1.40	DCT	20190118	104	ABAB	1.25	DCT
20170216	50	ABBA	1.19	DCT	20171123	143	AB	1.44	DCT	20190126	113	AB	1.19	DCT
20170910	130	AB	1.73	DCT	20171209	120	AB	1.58	DCT	20190127	184	AB	1.20	DCT
20170911	72	ABBA	1.75	DCT	20171214	144	AB	1.35	DCT	20190128	90	ABBA	1.25	DCT
20170912	124	AB	1.79	DCT	20180101	172	AB	1.21	DCT	20190130	100	ABAB	1.33	DCT
20170915	118	AB	1.60	DCT	20180105	123	AB	1.19	DCT	20190209	146	AB	1.31	DCT
20170929	186	AB	1.27	DCT	20180114	134	AB	1.19	DCT	20190211	130	AB	1.25	DCT
20170930	178	AB	1.29	DCT	20180123	156	AB	1.20	DCT	20190304	135	AB	1.20	DCT
20171001	170	AB	1.27	DCT	20180124	177	AB	1.19	DCT	20190305	118	AB	1.20	DCT
20171002	122	AB	1.33	DCT	20180922	103	AB	1.46	DCT	20190309	82	ABAB	1.21	DCT
20171003	114	AB	1.37	DCT	20180929	100	AB	1.75	DCT	20190316	137	AB	1.25	DCT
20171004	111	AB	1.37	DCT										
						HD 2	6257 (H Band)							
20161110	120	AB	1.29	DCT	20170911	113	AB	1.22	DCT	20171011	176	AB	1.46	DCT
20161125	186	AB	1.56	DCT	20170912	112	AB	1.25	DCT	20171018	103	AB	1.21	DCT
20161207	107	AB	1.39	DCT	20170915	114	AB	1.22	DCT	20171021	143	AB	1.24	DCT
20161219	210	AB	1.33	DCT	20170929	210	AB	1.61	DCT	20171028	123	AB	1.25	DCT
20161220	66	AB	1.23	DCT	20170930	189	AB	1.59	DCT	20171029	121	AB	1.25	DCT
20170106	94	AB	1.88	DCT	20171001	161	AB	1.62	DCT	20171111	111	AB	1.29	DCT
20170128	122	AB	1.27	DCT	20171002	105	AB	1.21	DCT	20171115	199	AB	2.13	DCT
20170214	139	BA	1.22	DCT	20171003	119	AB	1.28	DCT	20171119	118	AB	1.39	DCT
20170215	187	AB	1.21	DCT	20171004	111	AB	1.25	DCT	20171209	119	AB	1.24	DCT
20170905	49	ABBA	1.52	DCT	20171005	115	AB	1.36	DCT	20171213	108	AB	1.35	DCT
20170906	157	AB	1.70	DCT	20171006	116	AB	1.60	DCT	20171214	132	AB	1.46	DCT
20170910	111	AB	1.26	DCT	20171007	124	AB	1.23	DCT	20180112	101	AB	1.27	DCT

Note.

^a Median S/N. *H* band from orders 104, 111, 112, 114, 119, and 120. *K* band from orders 74, 75, 76, and 77.

Stahl et al.

Table B2
IGRINS Observations for Planet Hosts

					IOKIN	3 Observa	tions for Planet	HOSIS						
UT Date	S/N ^a	Nod Seq.	AM	Facility	UT Date	S/N ^a	Nod Seq.	AM	Facility	UT Date	S/N ^a	Nod Seq.	AM	Facility
(yyyymmdd_#) ^b					(yyyymmdd_#) ^b					(yyyymmdd_#) ^b				
(1)	(2)	(3)	(4)	(5)	(1)	(2)	(3)	(4)	(5)	(1)	(2)	(3)	(4)	(5)
						HD 1897	33 (K Band)							
20150502_0087	145	ABBA	1.83	McD	20160721_0120	240	ABBA	1.15	McD	20161013_0138	106	ABBA	1.22	DCT
20150502_0092	73	ABBAAB	1.56	McD	20160721_0124	241	ABBA	0.11	McD	20161013_0142	103	ABBA	1.23	DCT
20150502_0104	47	ABBA	1.20	McD	20161013_0038	110	ABBA	1.05	DCT	20161013_0146	73	ABBA	1.25	DCT
20150926_0066	134	ABBA	1.12	McD	20161013_0042	121	ABBA	1.05	DCT	20161013_0150	78	ABBA	1.26	DCT
20150930_0065	128	ABBA	1.23	McD	20161013_0046	120	ABBA	1.05	DCT	20161013_0154	81	ABBA	1.27	DCT
20150930_0069	124	ABBA	1.26	McD	20161013_0050	118	ABBA	1.06	DCT	20161025_0043	123	ABBA	1.06	DCT
20150930_0073	122	ABBA	1.29	McD	20161013_0054	121	ABBA	1.06	DCT	20161025_0047	128	ABBA	1.06	DCT
20150930_0077	120	ABBA	1.32	McD	20161013_0058	113	ABBA	1.06	DCT	20161025_0051	139	ABBA	1.07	DCT
20160502_0094	245	ABBA	1.76	McD	20161013_0062	113	ABBA	1.07	DCT	20161025_0055	135	ABBA	1.07	DCT
20160502_0098	239	ABBA	1.60	McD	20161013_0066	111	ABBA	1.08	DCT	20161025_0059	118	ABBA	1.08	DCT
20160502_0106	262	ABBA	1.33	McD	20161013_0070	103	ABBA	1.08	DCT	20161025_0063	146	ABBA	1.09	DCT
20160502_0110	257	ABBA	1.25	McD	20161013_0074	114	ABBA	1.08	DCT	20161025_0067	131	ABBA	1.09	DCT
20160502_0114	257	ABBA	1.18	McD	20161013_0078	104	ABBA	1.09	DCT	20161025_0071	109	ABBA	1.10	DCT
20160502_0118	269	ABBA	1.13	McD	20161013_0082	116	ABBA	1.10	DCT	20161025_0075	139	ABBA	1.11	DCT
20160502_0126	234	ABBA	1.06	McD	20161013_0086	113	ABBA	1.11	DCT	20161025_0087	141	ABBA	1.16	DCT
20160502_0130	249	ABBAAB	1.03	McD	20161013_0090	111	ABBA	1.12	DCT	20161025_0091	146	ABBA	1.17	DCT
20160721_0049	258	ABBA	0.21	McD	20161013_0094	116	ABBA	1.12	DCT	20161025_0095	147	ABBA	1.18	DCT
20160721_0053	262	ABBA	0.75	McD	20161013_0098	106	ABBA	1.13	DCT	20161025_0099	149	ABBA	1.20	DCT
20160721_0057	266	ABBA	0.13	McD	20161013_0102	95	ABBA	1.14	DCT	20161025_0103	150	ABBA	1.21	DCT
20160721_0061	273	ABBA	0.64	McD	20161013_0106	98	ABBA	1.14	DCT	20161025_0107	143	ABBA	1.22	DCT
20160721_0065	275	ABBA	1.15	McD	20161013_0110	95	ABBA	1.15	DCT	20161025_0119	144	ABBA	1.29	DCT
20160721_0082	264	ABBA	0.53	McD	20161013_0114	95	ABBA	1.16	DCT	20161025_0123	145	ABBA	1.30	DCT
20160721_0086	268	ABBA	0.51	McD	20161013_0118	105	ABBA	1.17	DCT	20161025_0127	145	ABBA	1.32	DCT
20160721_0090	266	ABBA	0.01	McD	20161013_0122	108	ABBA	1.18	DCT	20161025_0131	149	ABBA	1.34	DCT
20160721_0094	261	ABBA	1.01	McD	20161013_0126	93	ABBA	1.19	DCT	20161025_0135	156	ABBA	1.36	DCT
20160721_0112	227	ABBA	0.03	McD	20161013_0130	100	ABBA	1.20	DCT	20161025_0139	151	ABBA	1.38	DCT
20160721_0116	239	ABBA	-0.47	McD	20161013_0134	110	ABBA	1.21	DCT	20170907_0049	135	ABBA	1.03	DCT
						au Boo	(H Band)							
20150106_0149	448	ABBA	1.46	McD	20150429_0112	676	ABBA	1.03	McD	20160222_0248	176	ABBA	1.16	McD
20150106_0153	291	ABBA	1.42	McD	20150429_0116	690	ABBA	1.03	McD	20160222_0252	204	ABBA	1.18	McD
20150106_0169	316	ABBA	1.13	McD	20150429_0120	689	ABBA	1.03	McD	20160222_0256	199	ABBA	1.19	McD
20150126_0082	187	ABBA	1.08	McD	20150429_0124	671	ABBA	1.03	McD	20160222_0260	200	ABBA	1.21	McD
20150126_0086	264	ABBA	1.07	McD	20150429_0128	682	ABBA	1.03	McD	20160222_0264	191	ABBA	1.22	McD
20150126_0090	233	ABBA	1.07	McD	20150429_0136	689	ABBA	1.05	McD	20160224_0116	298	ABBA	1.21	McD
20150126_0094	287	ABBA	1.06	McD	20150429_0140	673	ABBA	1.06	McD	20160224_0120	303	ABBA	1.20	McD
20150126_0098	331	ABBA	1.05	McD	20150429_0144	664	ABBA	1.07	McD	20160224_0124	292	ABBA	1.18	McD
20150126_0102	321	ABBA	1.05	McD	20150429_0148	602	ABBA	1.09	McD	20160224_0130	273	ABBA	1.17	McD
20150126_0130	276	ABBA	1.03	McD	20150429_0152	589	ABBA	1.11	McD	20160224_0134	292	ABBA	1.15	McD
20150126_0134	292	ABBA	1.04	McD	20150501_0129	505	ABBA	1.06	McD	20160224_0138	299	ABBA	1.14	McD
20150126_0138	324	ABBA	1.04	McD	20150524_0055	287	ABBA	1.15	McD	20160224_0142	299	ABBA	1.13	McD
20150127_0168	326	ABBA	1.11	McD	20150524_0059	294	ABBA	1.13	McD	20160224_0146	300	ABBA	1.12	McD
20150127_0172	328	ABBA	1.10	McD	20150524_0063	304	ABBA	1.12	McD	20160224_0150	294	ABBA	1.11	McD
20150127_0176	326	ABBA	1.09	McD	20150524_0067	293	ABBA	1.11	McD	20160224_0154	305	ABBA	1.10	McD

Stahl

et

<u>a</u>

Stahl et al.

Table B2 (Continued)

UT Date	S/N^{a}	Nod Seq.	AM	Facility	UT Date	S/N^{a}	Nod Seq.	AM	Facility	UT Date	$\mathrm{S/N}^{\mathrm{a}}$	Nod Seq.	AM	Facility
(yyyymmdd_#) ^b					(yyyymmdd_#) ^b					(yyyymmdd_#) ^b				
(1)	(2)	(3)	(4)	(5)	(1)	(2)	(3)	(4)	(5)	(1)	(2)	(3)	(4)	(5)
20150306_0128	447	ABBA	1.06	McD	20150702_0055	295	ABBA	1.04	McD	20160225_0175	316	ABBA	1.03	McD
20150306_0140	112	ABBA	1.03	McD	20150702_0059	298	ABBA	1.05	McD	20160225_0179	313	ABBA	1.03	McD
20150306_0144	171	ABBA	1.04	McD	20150702_0064	304	ABBA	1.06	McD	20160225_0183	315	ABBA	1.03	McD
20150306_0148	236	ABBA	1.04	McD	20150703_0059	283	ABBA	1.07	McD	20160225_0187	324	ABBA	1.03	McD
20150306_0152	208	ABBA	1.05	McD	20150703_0063	258	ABBA	1.08	McD	20160225_0191	314	ABBA	1.03	McD
20150306_0156	180	ABBA	1.07	McD	20150703_0067	251	ABBA	1.09	McD	20160225_0195	319	ABBA	1.03	McD
20150306_0160	186	ABBA	1.08	McD	20150703_0071	286	ABBA	1.10	McD	20160225_0199	307	ABBA	1.03	McD
20150306_0173	80	ABBA	1.17	McD	20160202_0156	275	ABBA	7.53	McD	20160225_0203	311	ABBA	1.03	McD
20150306_0177	72	ABBA	1.20	McD	20160202_0160	285	ABBA	-1.00	McD	20160225_0207	316	ABBA	1.03	McD
20150306_0181	39	ABBA	1.24	McD	20160202_0164	281	ABBA	5.25	McD	20160225_0211	320	ABBA	1.03	McD
20150306_0185	55	ABBA	1.29	McD	20160202_0168	260	ABBA	6.73	McD	20160225_0215	323	ABBA	1.04	McD
20150306_0189	111	ABBA	1.34	McD	20160202_0172	280	ABBA	6.35	McD	20160225_0219	317	ABBA	1.04	McD
20150331_0115	265	ABBA	1.05	McD	20160202_0176	263	ABBA	6.50	McD	20160225_0223	316	ABBA	1.04	McD
20150331_0119	285	ABBA	1.05	McD	20160202_0180	284	ABBA	6.27	McD	20160225_0232	295	ABBA	1.07	McD
20150331_0123	275	ABBA	1.04	McD	20160202_0184	277	ABBA	2.53	McD	20160225_0236	289	ABBA	1.07	McD
20150331_0127	246	ABBA	1.04	McD	20160202_0188	291	ABBA	5.88	McD	20160225_0240	288	ABBA	1.08	McD
20150331_0131	296	ABBA	1.03	McD	20160202_0192	286	ABBA	5.75	McD	20160225_0244	307	ABBA	1.09	McD
20150331_0135	284	ABBA	1.03	McD	20160202_0220	251	ABBA	-1.00	McD	20160225_0248	290	ABBA	1.09	McD
20150331_0139	303	ABBA	1.03	McD	20160202_0224	263	ABBA	6.03	McD	20160225_0252	306	ABBA	1.10	McD
20150331_0143	301	ABBA	1.03	McD	20160202_0228	246	ABBA	8.53	McD	20160225_0256	302	ABBA	1.11	McD
20150331_0147	276	ABBA	1.03	McD	20160202_0232	248	ABBA	8.60	McD	20160226_0084	306	ABBA	1.13	McD
20150331_0151	280	ABBA	1.03	McD	20160202_0236	288	ABBA	3.80	McD	20160226_0088	319	ABBA	1.12	McD
20150331_0159	266	ABBA	1.03	McD	20160202_0240	284	ABBA	8.60	McD	20160226_0092	309	ABBA	1.11	McD
20150331_0163	252	ABBA	1.03	McD	20160202_0244	289	ABBA	6.20	McD	20160226_0096	317	ABBA	1.10	McD
20150331_0167	247	ABBA	1.04	McD	20160203_0132	323	ABBA	1.33	McD	20160226_0100	309	ABBA	1.10	McD
20150331_0171	228	ABBA	1.04	McD	20160203_0136	318	ABBA	0.80	McD	20160226_0104	314	ABBA	1.09	McD
20150331_0175	232	ABBA	1.04	McD	20160203_0140	327	ABBA	0.80	McD	20160226_0108	316	ABBA	1.08	McD
20150331_0179	235	ABBA	1.05	McD	20160203_0144	319	ABBA	-0.40	McD	20160226_0112	308	ABBA	1.07	McD
20150331_0183	230	ABBA	1.05	McD	20160203_0148	306	ABBA	-0.38	McD	20160226_0116	312	ABBA	1.07	McD
20150331_0187	257	ABBA	1.06	McD	20160203_0152	316	ABBA	1.50	McD	20160226_0120	316	ABBA	1.06	McD
20150331_0191	236	ABBA	1.06	McD	20160203_0156	323	ABBA	1.58	McD	20160226_0128	311	ABBA	1.04	McD
20150331_0195	257	ABBA	1.07	McD	20160203_0160	311	ABBA	1.60	McD	20160226_0132	316	ABBA	1.04	McD
20150331_0203	265	ABBA	1.11	McD	20160203_0164	330	ABBA	1.60	McD	20160226_0136	307	ABBA	1.04	McD
20150331_0207	217	ABBA	1.12	McD	20160203_0168	327	ABBA	0.33	McD	20160226_0140	315	ABBA	1.03	McD
20150331_0211	235	ABBA	1.13	McD	20160203_0172	335	ABBA	1.70	McD	20160226_0144	308	ABBA	1.03	McD
20150331_0215	218	ABBA	1.14	McD	20160203_0176	333	ABBA	-0.33	McD	20160226_0148	316	ABBA	1.03	McD
20150331_0219	224	ABBA	1.16	McD	20160203_0180	334	ABBA	1.17	McD	20160226_0152	317	ABBA	1.03	McD
20150331_0223	213	ABBA	1.17	McD	20160203_0184	341	ABBA	1.90	McD	20160226_0156	311	ABBA	1.03	McD
20150401_0117	347	ABBA	1.05	McD	20160203_0188	347	ABBA	2.25	McD	20160226_0160	315	ABBA	1.03	McD
20150401_0121	335	ABBA	1.05	McD	20160203_0192	344	ABBA	2.75	McD	20160226_0164	317	ABBA	1.03	McD
20150401_0125	327	ABBA	1.04	McD	20160203_0196	346	ABBA	-0.03	McD	20160226_0168	319	ABBA	1.03	McD
20150401_0129	346	ABBA	1.04	McD	20160203_0200	335	ABBA	0.15	McD	20160226_0172	314	ABBA	1.03	McD
20150401_0133	314	ABBA	1.03	McD	20160203_0204	329	ABBA	2.55	McD	20160226_0176	314	ABBA	1.03	McD
20150401_0137	339	ABBA	1.03	McD	20160222_0064	242	ABBA	1.30	McD	20160226_0180	310	ABBA	1.03	McD
20150401_0141	352	ABBA	1.03	McD	20160222_0068	246	ABBA	1.28	McD	20160226_0184	315	ABBA	1.04	McD
20150401_0145	349	ABBA	1.03	McD	20160222_0072	247	ABBA	1.26	McD	20160226_0192	313	ABBA	1.05	McD

Table B2 (Continued)

UT Date	S/N ^a	Nod Seq.	AM	Facility	UT Date	S/N ^a	Nod Seq.	AM	Facility	UT Date	S/N ^a	Nod Seq.	AM	Facility
(yyyymmdd_#) ^b (1)	(2)	(3)	(4)	(5)	(yyyymmdd_#) ^b (1)	(2)	(3)	(4)	(5)	$(yyyymmdd_{\#})^b$ (1)	(2)	(3)	(4)	(5)
20150401_0149	352	ABBA	1.03	McD	20160222_0076	249	ABBA	1.24	McD	20160226_0196	305	ABBA	1.06	McD
20150401_0153	340	ABBA	1.03	McD	20160222_0080	249	ABBA	1.23	McD	20160226_0200	306	ABBA	1.07	McD
20150401_0157	333	ABBA	1.03	McD	20160222_0084	244	ABBA	1.21	McD	20160226_0206	313	ABBA	1.07	McD
20150401_0165	338	ABBA	1.03	McD	20160222_0092	238	ABBA	1.15	McD	20160226_0210	323	ABBA	1.08	McD
20150401_0169	356	ABBA	1.03	McD	20160222_0096	235	ABBA	1.14	McD	20160226_0214	321	ABBA	1.09	McD
20150401_0173	355	ABBA	1.04	McD	20160222_0100	239	ABBA	1.13	McD	20160226_0218	319	ABBA	1.10	McD
20150401_0177	358	ABBA	1.04	McD	20160222_0104	239	ABBA	1.12	McD	20160226_0222	308	ABBA	1.11	McD
20150401_0181	353	ABBA	1.04	McD	20160222_0108	248	ABBA	1.10	McD	20160226_0226	319	ABBA	1.12	McD
20150401_0185	341	ABBA	1.05	McD	20160222_0112	248	ABBA	1.09	McD	20160226_0230	311	ABBA	1.13	McD
20150401_0189	346	ABBA	1.05	McD	20160222_0120	225	ABBA	1.07	McD	20160226_0234	316	ABBA	1.14	McD
20150401_0193	342	ABBA	1.06	McD	20160222_0124	227	ABBA	1.06	McD	20160226_0242	315	ABBA	1.18	McD
20150401_0197	340	ABBA	1.06	McD	20160222_0128	231	ABBA	1.06	McD	20160226_0246	306	ABBA	1.19	McD
20150401_0201	315	ABBA	1.07	McD	20160222_0132	221	ABBA	1.05	McD	20160226_0250	310	ABBA	1.21	McD
20150401_0205	355	ABBA	1.07	McD	20160222_0136	233	ABBA	1.05	McD	20160226_0254	315	ABBA	1.22	McD
20150401_0209	344	ABBA	1.08	McD	20160222_0140	235	ABBA	1.04	McD	20160226_0258	316	ABBA	1.24	McD
20150401_0213	354	ABBA	1.09	McD	20160222_0144	215	ABBA	1.04	McD	20160324_0078	261	ABBA	1.16	McD
20150428_0101	307	ABBA	1.23	McD	20160222_0148	221	ABBA	1.04	McD	20160324_0082	243	ABBA	1.15	McD
20150428_0105	292	ABBA	1.21	McD	20160222_0152	220	ABBA	1.03	McD	20160324_0086	246	ABBA	1.14	McD
20150428_0109	302	ABBA	1.20	McD	20160222_0156	219	ABBA	1.03	McD	20160324_0090	248	ABBA	1.13	McD
20150428_0113	310	ABBA	1.18	McD	20160222_0160	219	ABBA	1.03	McD	20160324_0094	242	ABBA	1.11	McD
20150428_0117	304	ABBA	1.17	McD	20160222_0164	208	ABBA	1.03	McD	20160324_0098	251	ABBA	1.10	McD
20150428_0121	306	ABBA	1.16	McD	20160222_0168	198	ABBA	1.03	McD	20160324_0107	263	ABBA	1.07	McD
20150428_0125	314	ABBA	1.14	McD	20160222_0172	210	ABBA	1.03	McD	20160324_0111	257	ABBA	1.06	McD
20150428_0129	313	ABBA	1.13	McD	20160222_0176	209	ABBA	1.03	McD	20160324_0115	259	ABBA	1.06	McD
20150428_0133	311	ABBA	1.12	McD	20160222_0180	217	ABBA	1.03	McD	20160324_0119	265	ABBA	1.05	McD
20150428_0137	303	ABBA	1.11	McD	20160222_0184	205	ABBA	1.03	McD	20160324_0123	261	ABBA	1.05	McD
20150428_0146	314	ABBA	1.07	McD	20160222_0188	202	ABBA	1.03	McD	20160324_0127	263	ABBA	1.04	McD
20150428_0150	324	ABBA	1.07	McD	20160222_0192	206	ABBA	1.03	McD	20160324_0131	262	ABBA	1.04	McD
20150428_0154	317	ABBA	1.06	McD	20160222_0196	204	ABBA	1.03	McD	20160324_0135	258	ABBA	1.04	McD
20150428_0158	326	ABBA	1.05	McD	20160222_0200	196	ABBA	1.04	McD	20160324_0139	257	ABBA	1.03	McD
20150428_0162	322	ABBA	1.05	McD	20160222_0208	202	ABBA	1.06	McD	20160324_0143	252	ABBA	1.03	McD
20150428_0166	307	ABBA	1.05	McD	20160222_0212	239	ABBA	1.06	McD	20160324_0147	249	ABBA	1.03	McD
20150428_0170	315	ABBA	1.04	McD	20160222_0216	195	ABBA	1.07	McD	20160324_0155	230	ABBA	1.03	McD
20150428_0174	317	ABBA	1.04	McD	20160222_0220	204	ABBA	1.07	McD	20160324_0159	240	ABBA	1.03	McD
20150428_0178	319	ABBA	1.04	McD	20160222_0224	227	ABBA	1.08	McD	20160324_0163	247	ABBA	1.03	McD
20150428_0182	316	ABBA	1.03	McD	20160222_0228	237	ABBA	1.09	McD	20160324_0167	238	ABBA	1.03	McD
20150429_0084	687	ABBA	1.12	McD	20160222_0232	219	ABBA	1.09	McD	20160324_0171	247	ABBA	1.04	McD
20150429_0088	691	ABBA	1.10	McD	20160222_0236	236	ABBA	1.10	McD	20160324_0175	248	ABBA	1.04	McD
20150429_0092	698	ABBA	1.08	McD	20160222_0244	179	ABBA	1.15	McD	20160324_0179	260	ABBA	1.05	McD
20150429_0096	697	ABBA	1.07	McD	20160222_0248	176	ABBA	1.16	McD	20160324_0183	244	ABBA	1.05	McD

Notes.^a Median S/N. H band from orders 104, 111, 112, 114, 119, and 120. K band from orders 74, 75, 76, and 77.

^b "#" is the IGRINS fits file number, for tracking multiple RVs per night.

Table B3Telluric Standard Stars

Designation	R.A. (hh:mm:ss)	Decl. (\pm dd:mm:ss)	SpTy	Assoc. Targets
10 Boo	13:58:38.921	+21:41:46.33	A0V	c
18 Ori	05:16:04.135	+11:20:28.88	A0V	ab
29 Vul	20:38:31.329	+21:12:04.38	A0V	d
30 Mon	08:25:39.632	-03:54:23.12	A0V	a
33 LMi	10:31:51.375	+32:22:46.41	A0V	a
5 Vul	19:26:13.246	+20:05:51.84	A0V	d
HD 121880	13:57:52.121	+16:12:07.52	A0V	c
HD 184787	19:34:18.191	+41:55:37.99	A0V	d
HD 31743	04:57:44.641	-13:42:17.93	A0V	a
HD 53205	07:04:20.175	+01:29:18.57	B9IV/V	ab
HD 63714	07:50:13.993	-01:27:32.12	A0V	a
HD 65158	07:57:25.860	+00:38:09.15	A0V	a
HR 1039	03:27:18.676	+12:44:07.03	A0V	ab
HR 1137	03:44:28.204	+20:55:43.45	A0V	b
HR 1234	04:01:14.832	+36:59:22.10	A0V	a
HR 1237	04:00:36.888	+17:17:47.97	A0V	ab
HR 1367	04:20:39.013	-20:38:22.63	A0V	a
HR 1482	04:41:24.128	+48:18:03.16	A0V	ab
HR 1558	04:54:51.243	+44:03:39.11	A0V	b
HR 1578	04:55:58.352	+05:23:56.49	A0V	b
HR 1724	05:16:41.039	+01:56:50.38	A0V	b
HR 2133	06:03:24.769	+11:40:51.84	A0V	a
HR 2315	06:25:46.528	+02:16:18.04	A0V	a
HR 2584	06:55:34.618	+08:19:27.43	A0V	a
HR 2893	07:34:04.962	+10:34:05.07	A0V	a
HR 7734	20:14:04.883	+36:36:17.56	A0V	d
HR 945	03:10:08.839	+27:49:11.16	A0V	b
k Tau	04:58:09.392	+25:03:01.47	A0V	ab
NSV12680	20:00:15.543	+29:55:14.25	A0V	d

Note. a: GJ 281; b: HD 26257; c: τ Boo A; d: HD 189733.

ORCID iDs

Asa G. Stahl https://orcid.org/0000-0002-0848-6960 Shih-Yun Tang https://orcid.org/0000-0003-4247-1401 Christopher M. Johns-Krull https://orcid.org/0000-0002-8828-6386

L. Prato https://orcid.org/0000-0001-7998-226X
Joe Llama https://orcid.org/0000-0003-4450-0368
Gregory N. Mace https://orcid.org/0000-0001-7875-6391
Jae Joon Lee https://orcid.org/0000-0003-0894-7824
Heeyoung Oh https://orcid.org/0000-0002-0418-5335
Daniel T. Jaffe https://orcid.org/0000-0003-3577-3540

References Akeson, R. L., Chen, X., Ciardi, D., et al. 2013, PASP, 125, 989 Alonso-Floriano, F. J., Sánchez-López, A., Snellen, I. A. G., et al. 2019, A&A, 621, A74 Astropy Collaboration, Price-Whelan, A. M., SipH ocz, B. M., et al. 2018, AJ, 156, 123 Bailer-Jones, C. A. L., Rybizki, J., Fouesneau, M., Mantelet, G., & Andrae, R. 2018, AJ, 156, 58 Bailey, John I. I., White, R. J., Blake, C. H., et al. 2012, ApJ, 749, 16 Bakos, G. Á, Pál, A., Latham, D. W., Noyes, R. W., & Stefanik, R. P. 2006, ApJL, 641, L57 Ballard, S. 2019, AJ, 157, 113 Bauer, F. F., Zechmeister, M., Kaminski, A., et al. 2020, A&A, 640, A50 Bean, J. L., Seifahrt, A., Hartman, H., et al. 2010, ApJ, 713, 410 Borsa, F., Scandariato, G., Rainer, M., et al. 2015, A&A, 578, A64 Bouchy, F., Udry, S., Mayor, M., et al. 2005, A&A, 444, L15 Box, M. 1965, CompJ, 8, 42

```
Brewer, J. M., Fischer, D. A., Valenti, J. A., & Piskunov, N. 2016, ApJS,
  225, 32
Brogi, M., Snellen, I. A. G., de Kok, R. J., et al. 2012, Natur, 486, 502
Butler, R. P., Marcy, G. W., Williams, E., et al. 1996, PASP, 108, 500
Butler, R. P., Marcy, G. W., Williams, E., Hauser, H., & Shirts, P. 1997, ApJL,
Butler, R. P., Vogt, S. S., Laughlin, G., et al. 2017, AJ, 153, 208
Butler, R. P., Wright, J. T., Marcy, G. W., et al. 2006, ApJ, 646, 505
Cale, B. L., Plavchan, P., Gagné, J., et al. 2018, arXiv:1803.04003
Carleo, I., Benatti, S., Lanza, A. F., et al. 2018, A&A, 613, A50
Clough, S. A., Shephard, M. W., Mlawer, E. J., et al. 2005, JQSRT, 91, 233
Collier Cameron, A., Bruce, V. A., Miller, G. R. M., Triaud, A. H. M. J., &
   Queloz, D. 2010, MNRAS, 403, 151
Crockett, C. J., Mahmud, N. I., Prato, L., et al. 2012, ApJ, 761, 164
David, T. J., Petigura, E. A., Luger, R., et al. 2019, ApJL, 885, L12
Dawson, R. I., & Johnson, J. A. 2018, ARA&A, 56, 175
Donati, J. F., Moutou, C., Malo, L., et al. 2016, Natur, 534, 662
Duarte, M., & Watanabe, R. 2018, BMClab / BMC, GitHub https://github.
  com/BMClab/BMC
Dumusque, X., Boisse, I., & Santos, N. C. 2014, ApJ, 796, 132
Endl, M., Cochran, W. D., Tull, R. G., & MacQueen, P. J. 2003, AJ, 126, 3099
Figueira, P., Pepe, F., Lovis, C., & Mayor, M. 2010, A&A, 515, A106
Fischer, D. A., & Valenti, J. 2005, ApJ, 622, 1102
Flagg, L., Johns-Krull, C. M., Nofi, L., et al. 2019, ApJL, 878, L37
Foreman-Mackey, D., Luger, R., Czekala, I., et al. 2020, exoplanet-dev/
   exoplanet v0.3.2, Zenodo, doi:https://doi.org/10.5281/zenodo.1998447
France, K., Loyd, R. O. P., Youngblood, A., et al. 2016, ApJ, 820, 89
Gaia Collaboration, Brown, A. G. A., Vallenari, A., et al. 2018, A&A, 616, A1
Głębocki, R., & Gnaciński, P. 2005, in Proc. 13th Cambridge Workshop on
   Cool Stars, Stellar Systems and the Sun, ed. F. Favata, G. A. J. Hussain, &
   B. Battrick (Noordwijk: ESA), 571
Gordon, I. E., Rothman, L. S., Hill, C., et al. 2017, JQSRT, 203, 3
Gray, R. O., Corbally, C. J., Garrison, R. F., McFadden, M. T., &
   Robinson, P. E. 2003, AJ, 126, 2048
Gray, R. O., Napier, M. G., & Winkler, L. I. 2001, AJ, 121, 2148
Greene, T. P., Tokunaga, A. T., Toomey, D. W., & Carr, J. B. 1993, Proc.
   SPIE, 1946, 313
Guerço, R., Cunha, K., Smith, V. V., et al. 2019, ApJ, 876, 43
Gullikson, K., Dodson-Robinson, S., & Kraus, A. 2014, AJ, 148, 53
Günther, M. N., Zhan, Z., Seager, S., et al. 2020, AJ, 159, 60
Hale, A. 1994, AJ, 107, 306
Hauschildt, P. H., Allard, F., Ferguson, J., Baron, E., & Alexander, D. R. 1999,
   ApJ, 525, 871
Henry, T. J., Jao, W.-C., Subasavage, J. P., et al. 2006, AJ, 132, 2360
Hinkle, K. H., Cuberly, R. W., Gaughan, N. A., et al. 1998, Proc. SPIE,
   3354, 810
Hojjatpanah, S., Figueira, P., Santos, N. C., et al. 2019, A&A, 629, A80
Houk, N., & Swift, C. 1999, Michigan Catalogue of Two-dimensional Spectral
   Types for the HD Stars, vol. 5 (Ann Arbor, MI: Univ. Michigan)
Huélamo, N., Figueira, P., Bonfils, X., et al. 2008, A&A, 489, L9
Huerta, M., Johns-Krull, C. M., Prato, L., Hartigan, P., & Jaffe, D. T. 2008,
   ApJ, 678, 472
Husser, T. O., Wende-von Berg, S., Dreizler, S., et al. 2013, A&A, 553, A6
Institute for Astronomy at KU Leuven 2018, IvSPythonRepository/spectra/
   tools.py, GitHub https://github.com/IvS-KULeuven/IvSPythonRepository/
   blob/master/spectra/tools.py
Johns-Krull, C. M. 2007, ApJ, 664, 975
Johns-Krull, C. M., McLane, J. N., Prato, L., et al. 2016, ApJ, 826, 206
Johnson, S. 2008, The NLopt Nonlinear-optimization Package https://github.
   com/stevengj/nlopt
Justesen, A. B., & Albrecht, S. 2019, A&A, 625, A59
Kaplan, K. F., Dinerstein, H. L., Oh, H., et al. 2017, ApJ, 838, 152
Kochukhov, O. P. 2007, in Proc. Int. Conf., Physics of Magnetic Stars, ed.
   I. I. Romanyuk, D. O. Kudryavtsev et al. (Moscow: Special Astrophys. Obs.
   Russian AS), 109
Kotani, T., Tamura, M., Suto, H., et al. 2014, Proc. SPIE, 9147, 914714
Kraus, A. L., Ireland, M. J., Cieza, L. A., et al. 2014, ApJ, 781, 20
Latouf, N., Wang, S., Plavchan, P., Cale, B., & Blake, C. 2020, AAS Meeting,
   235, 458.01
Lee, J.-J., Gullikson, K., & Kaplan, K. 2017, igrins/plp 2.2.0, Zenodo, doi:10.
   5281/zenodo.845059
Lépine, S., Hilton, E. J., Mann, A. W., et al. 2013, AJ, 145, 102
Livingston, J. H., Dai, F., Hirano, T., et al. 2018, AJ, 155, 115
Livingston, W., & Wallace, L. 1991, An Atlas of the Solar Spectrum in the
   Infrared from 1850 to 9000 cm-1 (1.1 to 5.4 micrometer), NSO Tech. Rep.
```

91-001

```
Llama, J., Cabrera, T., Luna, J., et al. 2019, AAS Meeting, 233, 247.32
Mace, G., Jaffe, D., Park, C., & Lee, J.-J. 2016a, Stellar radial velocities with
   IGRINS at McDonald Observatory, Zenodo, doi:10.5281/zenodo.56434
Mace, G., Kim, H., Jaffe, D. T., et al. 2016b, Proc. SPIE, 9908, 99080C
Mace, G., Sokal, K., Lee, J.-J., et al. 2018, Proc. SPIE, 10702, 107020Q
Mahadevan, S., Ramsey, L., Bender, C., et al. 2012, Proc. SPIE, 8446, 84461S
Mahmud, N. I., Crockett, C. J., Johns-Krull, C. M., et al. 2011, ApJ, 736, 123
Maldonado, J., Martínez-Arnáiz, R. M., Eiroa, C., Montes, D., &
   Montesinos, B. 2010, A&A, 521, A12
Mann, A. W., Newton, E. R., Rizzuto, A. C., et al. 2016, AJ, 152, 61
Marcy, G. W., Isaacson, H., Howard, A. W., et al. 2014, ApJS, 210, 20
Martin, D. V., Triaud, A. H. M. J., Udry, S., et al. 2019, A&A, 624, A68
Mayor, M., & Queloz, D. 1995, Natur, 378, 355
Morishima, R., Schmidt, M. W., Stadel, J., & Moore, B. 2008, ApJ, 685, 1247
Moutou, C., Dalal, S., Donati, J. F., et al. 2020, A&A, 642, A72
Nelder, J., & Mead, R. 1965, CompJ, 7, 308
Oelkers, R. J., Macri, L. M., Marshall, J. L., et al. 2016, AJ, 152, 75
Pang, X., Li, Y., Tang, S.-Y., Pasquato, M., & Kouwenhoven, M. B. N. 2020,
   ApJL, 900, L4
Pang, X., Li, Y., Yu, Z., et al. 2021, arXiv:2102.10508
Park, C., Jaffe, D. T., Yuk, I.-S., et al. 2014, Proc. SPIE, 9147, 91471D
Plavchan, P., Barclay, T., Gagné, J., et al. 2020, Natur, 582, 497
Plavchan, P., Latham, D., Gaudi, S., et al. 2015, arXiv:1503.01770
Popović, G. M., & Pavlović, R. 1996, BABel, 153, 57
Prato, L., Huerta, M., Johns-Krull, C. M., et al. 2008, ApJL, 687, L103
Rayner, J., Tokunaga, A., Jaffe, D., et al. 2016, Proc. SPIE, 9908, 990884
```

Robertson, P., Stefansson, G., Mahadevan, S., et al. 2020, ApJ, 897, 125

```
Rodler, F., Lopez-Morales, M., & Ribas, I. 2012, ApJL, 753, L25
Rothman, L. S., Jacquemart, D., Barbe, A., et al. 2005, JOSRT, 96, 139
Ryabchikova, T., Piskunov, N., Kurucz, R. L., et al. 2015, PhyS, 90, 054005
Sallum, S., Follette, K. B., Eisner, J. A., et al. 2015, Natur, 527, 342
Salvatier, J., Wiecki, T. V., & Fonnesbeck, C. 2016, PeerJ Computer Science,
Schöfer, P., Jeffers, S. V., Reiners, A., et al. 2019, A&A, 623, A44
Schweitzer, A., Passegger, V. M., Cifuentes, C., et al. 2019, A&A, 625, A68
Seifahrt, A., & Käufl, H. U. 2008, A&A, 491, 929
Skrutskie, M. F., Cutri, R. M., Stiening, R., et al. 2006, AJ, 131, 1163
Soubiran, C., Jasniewicz, G., Chemin, L., et al. 2018, A&A, 616, A7
Steinrueck, M. E., Parmentier, V., Showman, A. P., Lothringer, J. D., &
  Lupu, R. E. 2019, ApJ, 880, 14
Sterling, N. C., Dinerstein, H. L., Kaplan, K. F., & Bautista, M. A. 2016, ApJL,
  819, L9
Tang, S., Stahl, A. G., Johns-Krull, C. M., Prato, L., & Llama, J. 2021, JOSS,
  6, 3095
Tang, S.-Y., Pang, X., Yuan, Z., et al. 2019, ApJ, 877, 12
Theano Development Team, Al-Rfou, R., Alaine, G., et al. 2016, arXiv:1605.
Tran, Q. H., Bowler, B. P., Cochran, W. D., et al. 2021, AJ, 161, 173
Triaud, A. H. M. J. 2018, in Handbook of Exoplanets, ed. H. Deeg &
  J. Belmonte (Cham: Springer), 2
van Eyken, J. C., Ciardi, D. R., von Braun, K., et al. 2012, ApJ, 755, 42
Vanderburg, A., Mann, A. W., Rizzuto, A., et al. 2018, AJ, 156, 46
```

Wang, Y., Zhou, J.-l., Hui-gen, L., & Meng, Z. 2017, ApJ, 848, 20

Yuk, I.-S., Jaffe, D. T., Barnes, S., et al. 2010, Proc. SPIE, 7735, 77351M